THESIS

OPEN-PATH CAVITY RING-DOWN SPECTROSCOPY FOR THE DETECTION OF HYDROGEN CHLORIDE GAS AND PARTICLES IN A CLEANROOM ENVIRONMENT

Submitted by

Muhammad Bilal Khan

Department of Mechanical Engineering

In partial fulfillment of the requirements

For the Degree of Master of Science

Colorado State University

Fort Collins, Colorado

Fall 2024

Master's Committee:

Advisor: Azer P. Yalin

Christian L'Orange
Dylan Yost

ABSTRACT

OPEN-PATH CAVITY RING-DOWN SPECTROSCOPY FOR THE DETECTION OF HYDROGEN CHLORIDE GAS AND PARTICLES IN A CLEANROOM ENVIRONMENT

Semiconductor chips are the driving force behind the electronics industry, and modern technology depends on these vital chips to function. The size of these semiconductors has been steadily decreasing in accordance with Moore's law. The increasingly smaller feature sizes require very pristine cleanroom manufacturing environments to ensure minimal contamination from unwanted gases and particles. Two of the main contaminants to monitor in a cleanroom are gaseous hydrogen chloride (HCl) and airborne particles. HCl is a corrosive gas that affects the lifespan of equipment, infrastructure, and ventilation systems while also negatively impacting human health. Likewise, the presence of airborne particles is problematic since it can result in yield loss due to blockage of the inscription of miniature circuits on the wafers. Manufacturing must occur in spaces between ISO 3 to 8 (International Organization for Standardization) requiring precise monitoring of particles.

The overarching goal of the present research is to develop new cleanroom monitoring methods for HCl and particles based on novel laser instrumentation. An acrylic chamber with controlled inlet and outlet flow was constructed and utilized to simulate cleanroom conditions. This chamber allowed for controlled air flows mixed with HCl gas in the range of ~0-100 parts-per-million (ppm) or particles at ISO levels of ~≤3-9. Detection of both HCl and particles uses a single continuous-wave 1742 nm near-

infrared laser as a light source for open path cavity ring-down spectroscopy (CRDS). The compact laser system consists of a 60 cm cavity. High sensitivity detection of HCl is achieved by probing the 2-0 vibrational band of HCl (R(3) line). The CRDS system can accurately detect HCl with an Allan deviation of 0.15 ppb over a 10-minute duration. Several approaches for particle detection based on analyzing the small fluctuations in ring-down times caused by Mie scattering are examined. The most sensitive particle detection uses statistical analysis of ring-down times based on the 3^{rd} and 4^{th} standard moments allowing the detection of particles (diameter > 1 μm) at low concentrations down to ISO of approximately 5. The results provide a promising foundation for the development of open-path CRDS laser instrumentation for cleanroom monitoring.

ACKNOWLEDGEMENTS

I would like to express my gratitude to my advisor, Dr. Azer Yalin, for his support, guidance, and encouragement over the past three years. His insightful advice, patience, and dedication have been invaluable not only in the completion of this thesis but also throughout my journey as a graduate student. I am deeply appreciative of all the time and effort he invested in reviewing my work, offering constructive feedback, and guiding me toward becoming a better researcher. This thesis would not have been possible without his mentorship. I am also profoundly grateful to Dr. Christian L'Orange, for his significant contributions to this project. His expert guidance and willingness to offer assistance whenever needed were essential in bringing this research to fruition. His support, particularly in the technical aspects of the project, played a critical role in making this work possible. A special thanks goes to my fellow graduate student, Anthony Puga, for his support during the initial stages of this project. His mentorship and camaraderie in the lab were invaluable, and his guidance helped me navigate many challenges during the early phases of this work.

Finally, I would like to thank my family for their unconditional love, patience, and encouragement. Without their unwavering belief in me and their support during the ups and downs of this journey, I would not be where I am today. Their presence in my life has been a constant source of strength and motivation, and I dedicate this achievement to them.

TABLE OF CONTENTS

LIST OF FIGURES

CHAPTER 1: Introduction to Cleanroom Monitoring and Thesis Goals

Microelectronics fabrication plants are intricate and highly sophisticated structures that necessitate the use of advanced air circulation and control systems. The control and reduction of small particles have been a longstanding focus in the semiconductor industry. However, modern microelectronics technology has also introduced the need for stringent control of gas-phase contaminants known as airborne molecular contaminants (AMCs). These contaminants significantly impact product quality, manufacturing processes, and equipment functionality. In today's advanced semiconductor manufacturing, protection against airborne molecular contamination has become an indispensable requirement, as it is no longer feasible to produce high-performance semiconductors without adequate AMC mitigation measures [1]. These topics are further detailed below.

1.1 Cleanroom Overview

Semiconductors are the backbone of the multi-trillion-dollar electronics industry. The integrated circuits on these semiconductors have consistently decreased in their feature size to produce more efficient and faster chips. With such small feature sizes and limited room for error, the advanced manufacturing techniques required necessitate clean environments. Cleanroom monitoring refers to the process of continuous measurement and analysis of this controlled environment (cleanroom) as is frequently used in sectors such as pharmaceuticals, biotechnology, electronics, and aerospace [2], [3].

Particulate matter (PM) comprising dust, dirt, and other contaminants, can jeopardize the production of integrated circuits and semiconductor devices [4]. Even small concentrations of particulate contaminants or different gasses can lead to device failures, machine downtimes, and significant yield losses. Measuring gas concentrations and controlling emissions is crucial for meeting environmental and safety regulations. By employing robust PM and gas measurement techniques, semiconductor manufacturers can proactively identify potential sources of contamination or process deviations at an early stage and thus mitigate potential risks to the environment, ensure the safety of their workforce, prevent yield loss, ensure higher product quality while minimizing scrap and rework costs, and identify maintenance requirements promptly, such as equipment cleaning or filter replacement. Regular maintenance ensures optimal equipment functionality, minimizes downtime, and reduces the risk of defects [5]. The primary focus is monitoring particulate levels and AMCs. However, it may also be necessary to control other environmental parameters such as temperature, humidity, and pressure [2], [3].

The International Organization for Standardization (ISO) maintains classifications for cleanrooms based on the concentration of particles, as shown in Table 1 [6].

Table 1. Cleanroom classifications [ISO 1644-1] [6].

ISO Classification number (N)	Maximum allowable concentration limits (particles/m^3 of air) for particles equal to and greater than the considered sizes shown below					
	0.1 µm	**0.2 µm**	**0.3 µm**	**0.5 µm**	**1 µm**	**5 µm**
1	10					
2	100	24	10	4		
3	1000	237	102	35	8	
4	10000	2370	1020	352	83	
5	100000	23700	10200	3520	832	29
6	1000000	237000	102000	35200	8320	293
7				352000	83200	2930
8				3520000	832000	29300
9				35200000	8320000	293000

In addition to particles, there are also many different AMCs of interest, but two representative examples are the acidic gaseous molecules of hydrogen fluoride (HF) and hydrogen chloride (HCl). The latter is known to impact device fabrication yield through copper (Cu) electrode corrosion and due to particulate matter formation with ammonia molecules ($NH_4Cl(s)$) which leads to disconnection of circuits by blocking lines as shown in Figure 1(a) and (b) (from [7], [8]). Another example of an AMC is gaseous ammonia (NH_3) which affects the hygiene of optical surfaces of photolithography instrumentation and product (wafer) surfaces via particulate matter formation with anionic counter partners (e.g. SO_4^{2-}) and surface settlements [9], [10]. Given the problems caused by many of these gaseous species, one concludes that control and

monitoring of AMCs is a critical issue in cleanrooms for the semiconductor fabrication industry [9], [10], [11], [12].

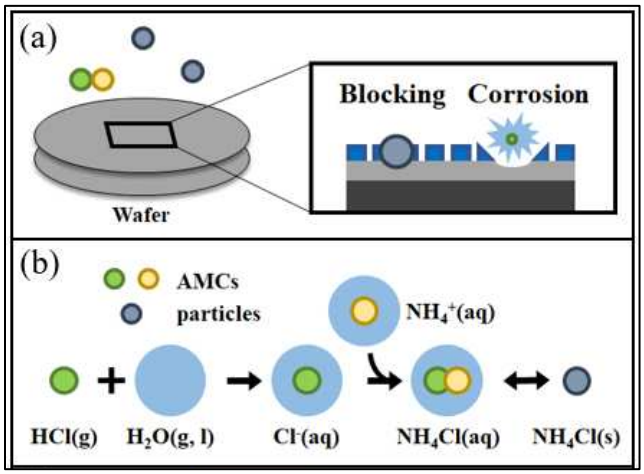

Figure 1: a) Example mechanism of yield loss by particle and AMC on the wafer surface, (b) Reaction between AMCs for particle formation, and (from [7], [8]).

Gas-to-particle conversion (GPC), e.g., the reactions between particles and ammonia (or hydrogen chloride) referred to above, along with other multiphase reactions, that produce nucleating particles has been a critical subject in atmospheric science due to its contribution to radiative forcing and climate change [13], [14], [15]. The presence of particles is also important to monitor for cleanroom purposes owing to the possibility of reduced yield as was mentioned in the previous paragraph. GPC requires a certain minimum level of humidity to provide water vapor that can coalesce to provide solvent that allows for enough collision frequency between acidic and basic molecules [15]. Lin et al. reported that the average Cl^- mass concentrations of particulate species in a cleanroom was 12% and the fractional distribution of HCl including its ion form, Cl^-, in the gas and particulate phases were about 50%, respectively [16]. Considering these values, it is expected that GPC and its reverse reaction with HCl may occur in cleanroom areas, which can then cause contamination of product surface.

Many manufacturing processes involve the utilization of halogen gas mixtures such as HCl. One critical issue in semiconductor manufacturing processes involves the adsorption of halogen gases on substrates during plasma etching or deposition processes [17]. Failure to adequately purge these gases from the process chamber can result in a significant presence of adsorbed chlorine-based species on the film surface. Their presence on the wafer can cause patterning defects such as localized blockage of subsequent plasma etching processes (Figure 2). Precise control over gas flow rates and composition ensures consistent and reliable outcomes, enhances production efficiency, and reduces the occurrence of defects.

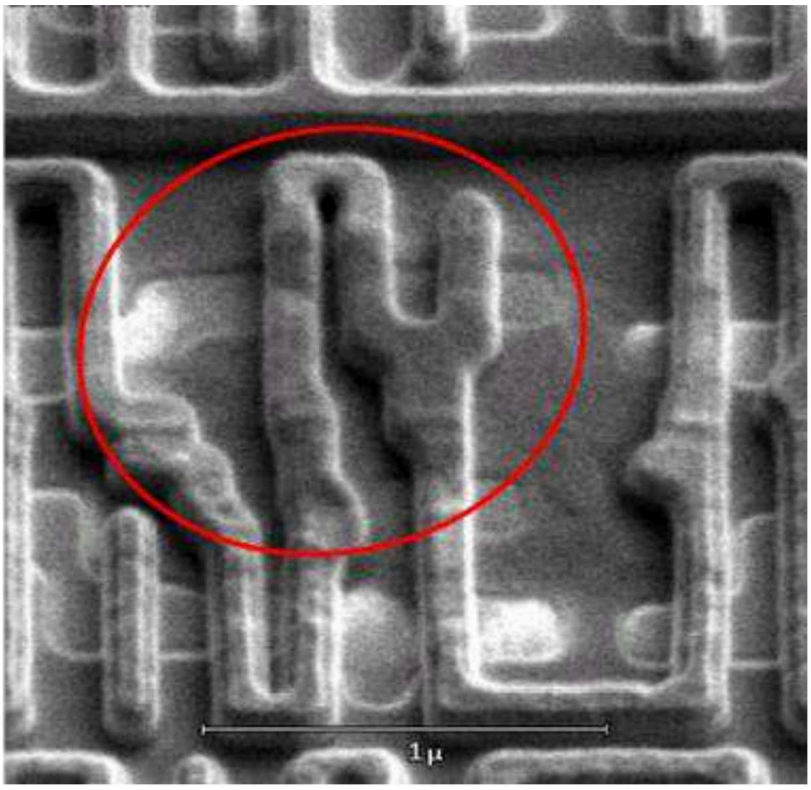

Figure 2: Localized blockage and corrosion caused by halogen adsorption on the surface of the wafer [17].

The continuous demand for performance increase in microelectronic devices has resulted in the utilization of novel materials. Notably, copper has emerged as a

substitute for aluminum in interconnects within high-performance devices. Unfortunately, the defectiveness of metal interconnects remains a significant concern in IC manufacturing processes. Pelissier et al. contaminated 200 nm Cu wafers with gaseous HCl and found that the presence of HCl results in the formation of copper chlorohydroxide which significantly restricts the functionality of the wafers [18].

A typical modern cleanroom setting is shown in Figure 3. The semiconductor industry has adopted a multilayered approach to contamination control in its processing operations to monitor the numerous sources of both internal and external AMC contamination. Within a typical semiconductor fabrication facility, various measures are implemented to mitigate AMC levels including the use of AMC filters at the ambient air inlet. Additionally, cleanroom areas are equipped with AMC filters placed on top of ceiling fan filter units. AMC filters typically use advanced filtration technologies to capture and remove molecular contaminants. Common technologies include adsorption, absorption, and chemical filtration [19]. Adsorption involves attracting and holding molecules onto the surface of a solid material. Activated carbon is a commonly used adsorbent in AMC filters due to its high surface area and ability to capture a wide range of organic molecules. In absorption, contaminants can be taken up by a liquid or solid material. Certain materials within the filter can absorb specific gases or vapors, preventing them from circulating in the air. Some AMC filters incorporate specific chemicals or reactive substances that can react with and neutralize harmful contaminants, which can be particularly effective in removing reactive gases. The demand for non-lithography tool protection against AMC has also increased steadily, particularly as the production of semiconductor devices progresses toward feature sizes

below 100 nm [20]. It is worth noting that in most fabs, the sub-fab and plenum spaces situated below and above the cleanrooms, respectively, are currently not filtered.

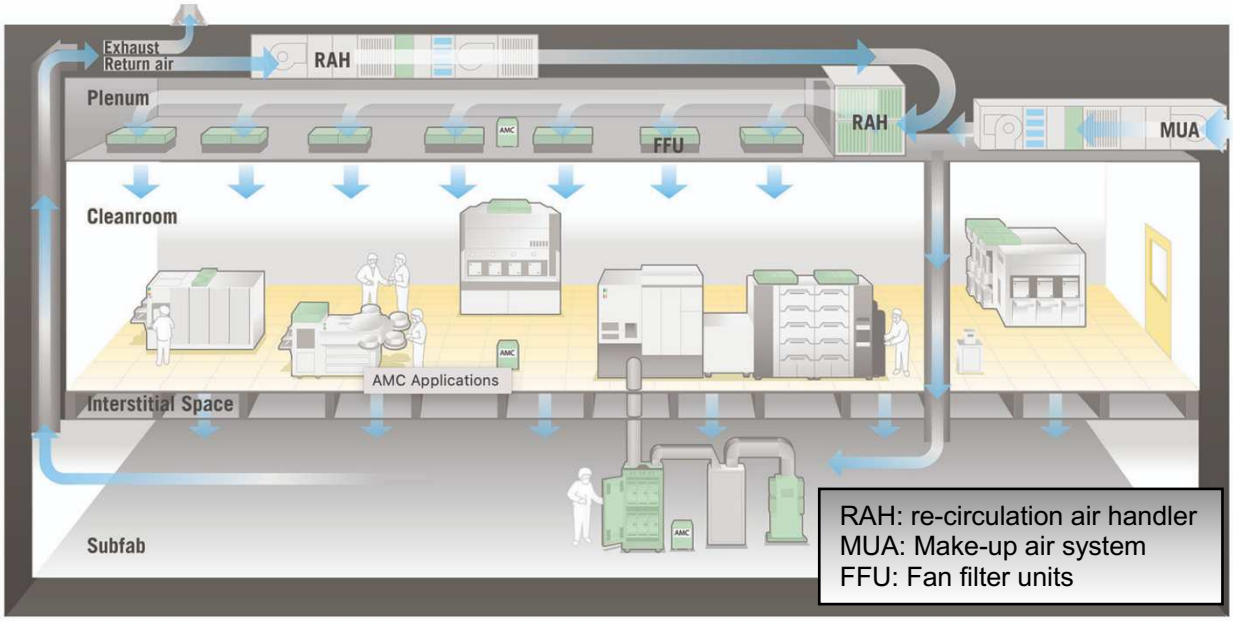

Figure 3: Schematic of typical cleanroom [21].

The design of current cleanrooms traces back to earlier industrial developments. In the early 1990s, researchers from IBM reported the issue of airborne chemical contamination [22] which prompted semiconductor companies to investigate the detrimental effects of AMCs on manufacturing processes. Several studies and preventative measures have been introduced to address this concern. For example, SEMATECH established AMC limits for the 0.25 µm feature-sizes process [23], and ISO 14644-8 provided guidelines for classifying AMCs in cleanrooms and controlled environments. These early studies offered valuable insights into the impact of AMCs on manufacturing processes, detection techniques, control methods, and related topics.

Between 1997 and 2008, 23 significant AMC incidents were reported by semiconductor plants globally, with one incident resulting in a staggering loss of

approximately US$100 million [24]. Consequently, establishing AMC-free facilities has become a critical requirement in semiconductor plants.

Although not the focus of this project (because the concentration of particles is already quite low in the cleanrooms), ultrafine particles can also cause breathing issues by penetrating the pulmonary alveolus [25]. Oxidative stress, which can lead to cardiovascular and neurological issues, can also be brought on by AMC inhalation. Several studies have also established a connection between exposure to PM and mortality [26], [27].

Our corporate sponsor, Samsung Electronics Corporation (SEC), sought a portable system capable of detecting both HCl and particles simultaneously. The compact design of our device enables easy mobility and facilitates placement on a mobile test platform within the cleanrooms, which makes it possible to monitor various sections of the cleanroom. Incorporating a gantry (Figure 4) enables real-time measurements to be taken in different areas of the cleanroom, aiding in identifying the original source of pollutants. This would require the detecting system to be compact and light enough to be maneuvered by the gantry. Our equipment is specifically designed to suit this gantry setup, offering rapid response times with minimal size and weight.

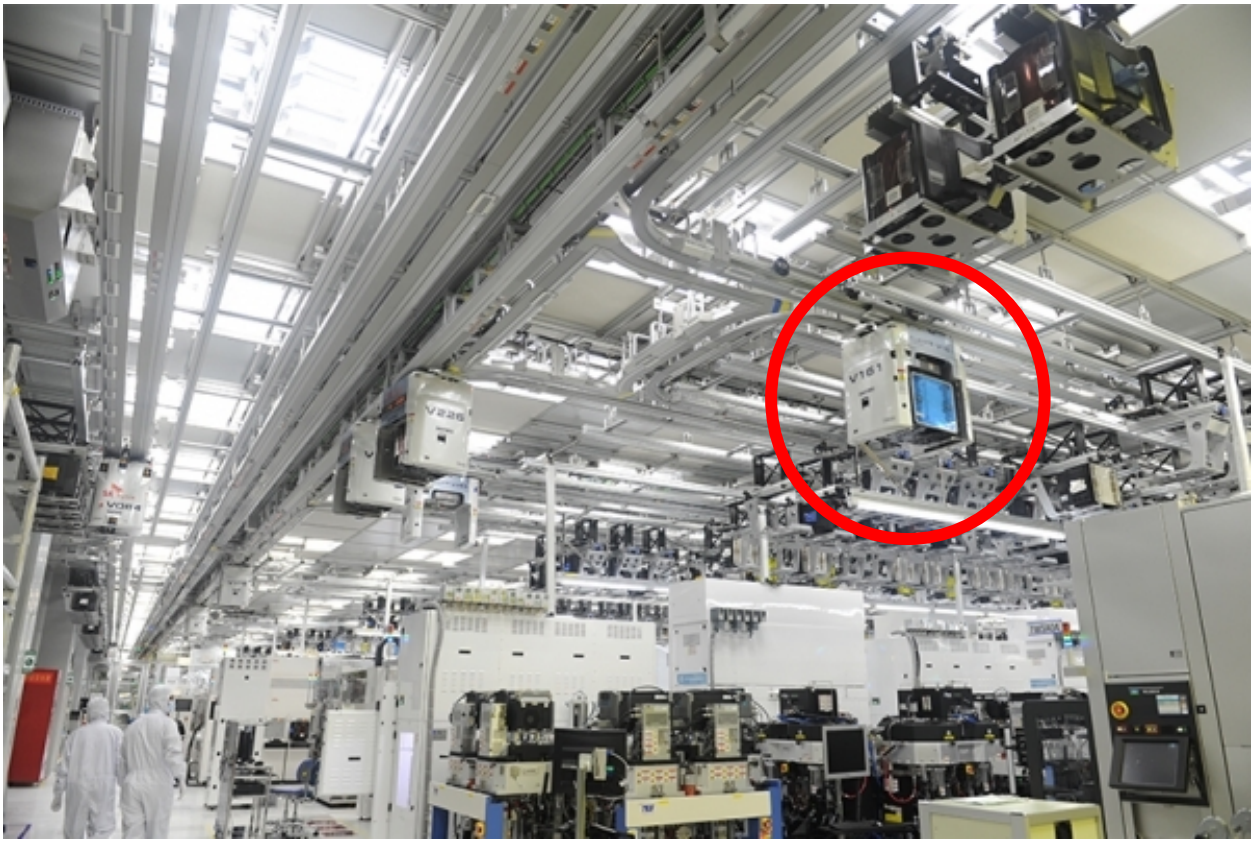

Figure 4: A gantry system (circled in red) helps in moving detection equipment within the facility allowing for wider area coverage for analysis and source tracing [28].

As further detailed below, the current industry standard for cleanroom particle monitoring is the use of optical counters that utilize the light-scattering properties of particles. However, these systems can only capture particle concentration for a specific size range of particles so multiple optical counters maybe needed to capture all ISO levels [29].

1.2 Instrumentation for Particle Measurement

Several types of instruments are currently used for particle measurement in cleanrooms. These instruments are designed to detect, count, and characterize particles based on size and concentration. The following is a short review of some of these instruments.

Optical Particle Counters (OPCs): Optical particle counters utilize the principle of Mie light scattering to detect and count particles in the air. They employ a light source, typically a laser, which illuminates the particles, and detectors measure the intensity of scattered light due to particles entrained in a gas flow streaming through the instrument. OPCs are capable of measuring particles in a wide size range (0.3 μm – 20 μm) and provide real-time data on particle concentration and size distribution [30]. These instruments are relatively inexpensive (thousands of dollars), compact, reliable and widely used. Our sponsor (SEC) desired a compact system for ease of mobility (gantry deployment) that can detect both HCl and particles together. OPCs, although applicable for detecting particles, cannot detect HCl or any other gases.

Condensation Particle Counters (CPCs): CPCs are specialized instruments that rely on the condensation of a working fluid onto particles as a means to increase their size for easier detection. These instruments can measure ultrafine particles down to sizes below 0.1 micrometers with high sensitivity. CPCs are generally more complex and expensive (as compared to OPCs) and are often used in research and advanced cleanroom environments where higher costs can be tolerated [31], [32].

Aerodynamic Particle Sizers (APS): APS measures aerosol particle size distribution using inertial impaction principles. Aerosol particles are accelerated through nozzles, traveling through a series of channels where particles of different sizes are separated based on their aerodynamic diameter. Upon exiting, particles impact a detector or surface, with the rate of impacts proportional to the number of particles at each size

[33], [34]. These instruments also tend to be rather complex and expensive for widespread cleanroom use.

Scanning Mobility Particle Sizers (SMPS): SMPS instruments combine a differential mobility analyzer (DMA) and a CPC to measure particles over a wide size range with high resolution. The DMA selects particles based on their electrical mobility, and the CPC counts the selected particles. SMPS is commonly used in research and development settings for detailed characterization of particle size distributions [35], [36].

1.3 Instrumentation for Gas-Phase Measurement

The project focuses on HCl detection specifically, but many other gases are of similar interest for AMC cleanroom detection so here we give a broad overview of instruments for gas detection. HCl detection examples are presented later. Multiple instruments can be used for gas phase detection, and we summarize those that are most widely used in related application areas. Where applicable, we comment on their possible use for cleanroom measurements.

Gas Chromatograph (GC): Gas chromatography is a widely employed technique for separating and analyzing gas mixtures. GC instruments utilize a combination of a stationary phase and a mobile phase (carrier gas) to separate individual gas components based on their different affinities for the stationary phase. Detectors such as flame ionization detectors (FID) or mass spectrometers (MS) are used to measure and identify the gases as they separate in time moving through the GC column [37].

GCs generally have rather long response times relative to what is desirable for cleanroom usage.

Mass Spectrometry (MS): Mass spectrometers are versatile instruments that can be used for gas-phase analysis. They ionize gaseous molecules and separate them based on their mass-to-charge ratio. Mass spectrometers accurately identify and quantify various gases and volatile compounds present in a gas sample [38]. Mass spectrometers have been used for cleanroom monitoring; however, they tend to be very bulky, massive and expensive.

Fourier Transform Infrared Spectroscopy (FTIR): FTIR instruments analyze gases based on their absorption of infrared radiation. By passing infrared light through a gas sample, the instrument measures the specific wavelengths that are absorbed, providing information about the chemical composition and concentration of the gases [39]. This technique has been used in some cleanroom monitoring applications, but challenges include sensitivity to temperature and humidity, and possible issues of sample contamination. These instruments also tend to be quite large and massive relative to the needs of SEC cleanrooms.

Photoionization Detector (PID): PIDs are commonly used to detect and measure volatile organic compounds (VOCs) in the gas phase. PIDs work by ionizing VOCs when they are exposed to ultraviolet (UV) light, and the resulting ions are measured to determine the concentration of the VOCs [40]. While PIDs are relatively compact and suited for

certain VOCs, they can suffer from cross-response (lack of specificity), which can be problematic when identifying specific cleanroom AMCs [41].

Electrochemical Gas Sensors: Electrochemical gas sensors are widely used for the detection and measurement of specific gases such as carbon monoxide (CO), hydrogen sulfide (H_2S), and oxygen (O_2). These sensors work based on the principle of electrochemical reactions between the target gas and the sensing electrode, producing an electrical signal proportional to the gas concentration [42]. The sensors are simple and inexpensive but tend to suffer from cross-response (lack of specificity). In many cases, their detection limits are also inadequate for trace AMC concentrations.

Non-Dispersive Infrared (NDIR) Analyzer: NDIR analyzers measure the concentration of gases based on their characteristic absorption of infrared light at specific wavelengths. They employ a source of infrared light, a detector, and an optical filter to selectively measure the absorption of the target gas [43]. These analyzers typically do not have the sensitivities needed for AMCs of interest for cleanrooms [43].

1.4 HCl Detection Need

The complex manufacturing process in integrated circuit chip industries requires more than 300 raw materials and solvents, many of which are highly toxic and hazardous [5]. One such solvent is HCl, a corrosive and toxic gas that can cause severe health hazards if inhaled in high concentrations. Early detection of HCl leaks or excessive levels can alert workers to take appropriate safety measures, to evacuate if necessary, and ultimately to prevent exposure-related injuries or illnesses.

The highly corrosive nature of HCl can also damage equipment, infrastructure, and ventilation systems [5], [18]. Gas phase detection of HCl helps identify potential corrosion risks, allowing for proactive maintenance and protection measures. Monitoring HCl levels in industrial exhaust gases can also prevent the corrosion of air pollution control devices, such as scrubbers or filters, ensuring their optimal performance and longevity.

HCl can also be released into the atmosphere because of an accident or during regular maintenance [5]. It is a significant contributor to acid rain formation when it reacts with water vapor in the air [44]. Hydrogen chloride is also a significant reservoir species for active halogens which can lead to the destruction of ozone in some areas of the troposphere [45]. By detecting and quantifying HCl gas in cleanrooms, one can assess the impact of inevitable emissions, evaluate air quality, and implement measures to mitigate its harmful effects on ecosystems. The project aimed to detect 1 ppb HCl as requested by SEC. In summary, there are multiple needs for HCl detection in cleanroom applications spanning human health, equipment and process integrity, and environmental concerns.

1.5 HCl Detection Instruments

Ion chromatography has been utilized to detect HCl. Keene et al. and Scheur et al. have demonstrated such approaches by using a mist chamber collector to collect gas-phase HCl into a solution and analyze the solution with high ion resolution ion chromatography [46], [47]. This method has a time resolution of tens of minutes or more, which is problematic for real-time monitoring, and is also limited by potential

interferences from other sources of chlorine [47]. A lower HCl detection limit of 13 pptv has been demonstrated by Keene et al using this technique [47].

An alternative method for detecting HCl involves the use of chemical ionization mass spectrometry (CIMS), as demonstrated in studies such as Roberts et al. (2010), Kim et al. (2008), and Veres et al. (2008) [48], [49]. CIMS instruments offer the advantage of rapid and highly sensitive detection of various species, making them suitable for deployment in both ground-based and aircraft-based measurements (as highlighted in Veres et al., 2008) [48]. However, there are potential limitations associated with these techniques, primarily related to their specificity, which relies on the intricate details of the ion chemistry involved. For instance, Marcy et al. (2004) reported the possibility of interference from water vapor when using CIMS [50]. Additionally, CIMS systems necessitate periodic zeroing and calibration procedures to maintain accuracy. Furthermore, the requirement for a sensitive mass spectrometer significantly increases the overall cost of the technique when compared to optical-based approaches.

In summary, while instruments for HCl detection are available, none are immediately suited for cleanroom monitoring due to factors such as sensitivity, measurement time, cost and maintenance requirements. Also, to the best of our knowledge, no one has attempted to measure HCl and particles simultaneously using the same equipment.

1.6 Thesis Objectives

The overarching goal of the present thesis research is to develop a measurement system that can quantitatively detect HCl (a prevalent AMC gas) down to levels of ~1

ppb while also detecting particles down to ISO ~5. The measurement system is intended for use in SEC cleanrooms including on their mobile measurement system so that relatively small size (<30 L) is also desired (see Figure 4). Accordingly, our approach centers around a custom-built open-path cavity ring-down spectroscopy sensor that is approximately 0.8x0.15x0.2 m in size. As will be further explained, cavity ring-down spectroscopy (CRDS) is a highly sensitive optical technique that is used for the measurement and analysis of trace gases and particles in various environments. We pursue the following objectives in support of our overall goal:

- Develop an instrumented test-bed chamber that can simulate cleanroom conditions including targeted particles and HCl gas (as representative AMC). The system should allow the quantitative setting of particle concentration (ISO level) and HCl concentrations.
- Build an open-path CRDS based on a tunable diode laser with a photodiode and an amplifier for laser beam loss detection. The CRDS should report cavity extinction (ring-down time) versus laser wavelength, from which absorption spectra (HCl concentration) and Mie scattering (particle information) can be inferred.
- Develop analysis methods for the CRDS instrument to infer HCl concentration based on absorption spectra, and particle concentration based on Mie scattering induced signal fluctuations.
- Perform multiple tests and optimize the instrument and analysis methods to obtain the most sensitive results for HCl and particle levels.

The layout of the thesis is as follows. Chapter 1 introduces the problem and provides background on cleanrooms, the needs and instrumentation for AMC and particle measurements, and thesis goals. Chapter 2 presents the technical details of CRDS, including its use for trace gas detection and particle concentration. Chapter 3 describes the experimental methods used to set up the CRDS and simulate cleanroom environments. An experimental testbed will be established to simulate cleanroom conditions, including a chamber with controlled gas and particle input flows and the use of a condensation particle counter (CPC) for reference measurements. Chapter 4 discusses the results and findings from the tests conducted. Data examples will be provided to illustrate the performance of the system. Finally, Chapter 5 summarizes the project's current status and future work that can improve the system.

CHAPTER 2: Introduction to Cavity Ring-Down Spectroscopy

2.1 Introduction and History

Cavity Ring-Down Spectroscopy (CRDS) has emerged as a powerful and versatile spectroscopic technique, driven by advancements in mirror reflectivity and the development of low-loss optical cavities. This chapter provides a comprehensive review of CRDS, discussing its fundamental principles and highlighting its remarkable sensitivity to loss. We emphasize discussion of both gas-phase detection as well as the more limited work on particles, as these are both required for our present thesis goals. The origins of CRDS trace back to the pioneering work of O'Keefe and Deacon [51], who demonstrated its effectiveness in measuring faint absorptions of molecular oxygen. Since then, CRDS has found extensive applications across various disciplines, and its family of related methods continues to evolve [52].

CRDS technology was initially developed as a means to measure the reflectivity of highly reflective dielectric mirrors (manufactured by ion sputtering techniques) [52], [53]. As the reflectivity of mirrors, denoted as R, approached unity (indicating maximum light reflection), accurately measuring this reflectivity became increasingly challenging. The conventional approach of measuring the minute difference in light intensity before and after reflection from the mirror proved impractical. While the transmission of the mirror, denoted as T, could be easily measured, it was important to account for the light lost due to absorption and scattering within the dielectric mirrors.

Researchers realized that a stable optical resonator could be constructed using a pair of such mirrors. They also recognized that the storage duration of light injected into

this cavity would be inversely proportional to the total loss per reflection, expressed as 1–R. Anderson et al.'s work [54] played a significant role in the development of CRDS. They activated the optical cavity using a laser and promptly deactivated it, observing the decay of intracavity light intensity through the transmission of light via one of the mirrors.

O'Keefe and Deacon in 1988 demonstrated that an instrument initially designed to measure mirror reflectivity could be repurposed to detect very weak visible absorptions arising from rare transitions of molecular oxygen in air [51]. Building on this foundation, O'Keefe, along with the research group led by Richard Saykally, subsequently published a series of papers over the next two years utilizing CRDS to identify electronic transitions in small metal clusters [55]. As a result, CRDS gained traction and began to be embraced by numerous research teams as a tool for molecular spectroscopy.

The CRDS technique allows for great sensitivity because the light in the cavity makes many passes within the optical cavity yielding a long effective path length in the order of kilometers. Any additional loss due to substances within the cavity, e.g., absorbing gases, results in a shorter ring-down time which can then be analyzed to yield the absorption spectrum and sample concentration.

2.2 Theory

2.2.1 Beer-Lambert law

The Beer-Lambert law, also known as the Beer-Lambert-Bouguer law, or simply Lambert's law, is a fundamental principle in spectroscopy that describes the relationship between the concentration of a substance in a solution and the amount of light it

absorbs [52]. The Beer-Lambert law describes how the intensity, *I*, of a light ray attenuates with distance due to sample absorption:

$$I = I_0 exp\ (-\mu(\nu)\mathrm{z}) \tag{1}$$

where I_0 is the initial light intensity of the light (at z=0), μ is the frequency-dependent absorption coefficient that depends also on sample concentration, and z is the distance traveled through the absorber.

More generally the absorption coefficient can be considered a "loss" or extinction coefficient. In cases, such as with gases and particles, where one has extinction due to both absorption and scattering, we can define a total extinction coefficient, μ, having dimension of inverse length expressed as:

$$\mu = \mu_{abs} + \mu_{scat} \tag{2}$$

where μ_{abs} represents the absorption coefficient and μ_{scat} represents the scattering coefficient (for example, due to Mie scattering loss caused by particles).

By measuring the extinction coefficient α and knowing other spectroscopic parameters, such as the absorption cross-section at the given wavelength and the path length z, it is possible to determine the concentration of the absorbing species in the sample using the Beer-Lambert law.

2.2.2 Basic CRDS Theory

In CRDS, the sample (causing absorption and/or scattering) is housed within a high-finesse optical cavity comprising two highly reflective mirrors facing each other. The sample to be analyzed is introduced into the cavity, and a laser pulse is injected into the cavity. The laser pulse undergoes multiple reflections between the mirrors during which it also gradually decays due to absorption and/or scattering by the sample.

As explained below, the decay times of the light in the cavity (as opposed to the direct intensity amplitude) are used to find sample concentrations via the Beer-Lambert Law.

The optical cavity used in CRDS is typically based on a Fabry-Perot interferometer configuration. It consists of two highly reflective mirrors facing each other, with a separation distance that determines the cavity length. The mirrors are designed to have very high reflectivity at the wavelength of interest, often exceeding 99.99%. A typical cavity setup is shown in Figure 5.

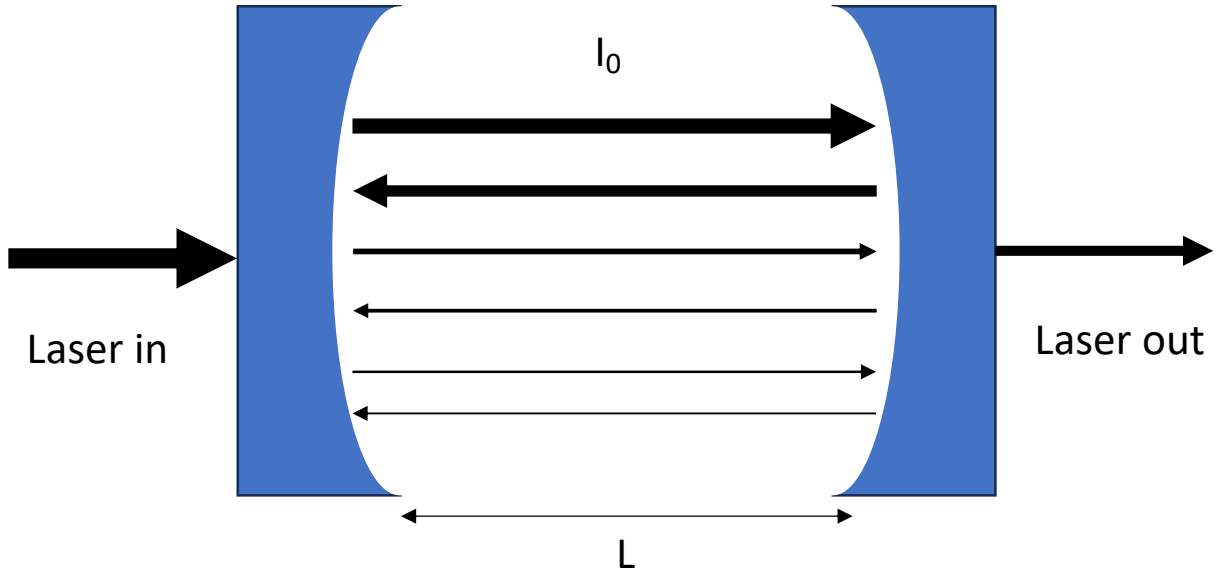

Figure 5: Schematic of a two-mirror optical cavity.

The decay of light intensity in the cavity (due only to the cavity mirror loss) follows an exponential behavior over time given by rate, k:

$$k = (1 - R)\frac{c}{L} \tag{3}$$

where c represents the speed of light and L signifies the distance between the mirrors. CRDS measurements are based on fitting for the cavity light decay time (referred to as the “ring-down time”), which is the time it takes for the light intensity to decrease to 1/e

of its initial value. In the absence of any absorbing sample, the decay time is referred to as the "empty cavity ring-down time", τ_0, found as the inverse of the rate mentioned above:

$$\tau_0 = \frac{L}{c(1-R)} \tag{4}$$

When a measurement is made, with an absorbing (or scattering) sample in the cavity, additional losses shorten the decay time. The resulting ring-down decay time, τ, in this case for extinction coefficient μ, is found as:

$$\tau = \frac{L}{c(1-R)+\mu L} \tag{5}$$

where μ is the extinction coefficient (which becomes equal to the absorption coefficient used in Beers Law for cases where there is only absorption).

From the point of view of the long effective path length earlier, the effective (1/e) distance travelled by light within the empty cavity is given by

$$L_{eff} = \tau_0 c = \frac{L}{(1-R)} \tag{6}$$

showing that the actual physical length of the cavity is effectively amplified by a factor of 1/(1-R).

Many CRDS experiments, including the work presented herein, use mirrors with reflectivity in excess of 99.99% (i.e., R>0.9999). The aforementioned mirrors will yield path length amplification of $>10^4$ which yields > 10 kms path length for typical physical cavity lengths of L=1 m. One can immediately see that the high mirror reflectivity greatly enhances the effective path length.

To make a measurement, the sample under investigation (gas containing AMC or particles) is introduced into the optical cavity. The interaction of the sample with the

laser beam causes a change in the decay time of the light. This change in decay time can readily be converted to give the absorption coefficient (μ) which can then be used to get the concentration of the given sample:

$$\mu = \frac{(1-\mathrm{R})}{L}\left(\frac{\tau_0 - \tau}{\tau}\right) \quad (7)$$

The CRDS laser source is typically tunable, allowing the selection of a specific wavelength matching the absorption line of the target gas. Common laser sources include distributed feedback diode, quantum cascade, or Ti:sapphire lasers.

The analyzed gas sample must be introduced into the optical cavity. Depending on the application, different methods can be employed. A sample cell or gas flow system is typically used to control the sample introduction and flow rate for gas-phase samples. No cell is required for gasses that are present in the ambient surrounding air as they will occupy as much of the cavity path as any other region within the room.

The detection system measures the decay of light intensity within the optical cavity. A high-speed photodetector, such as a photomultiplier tube or avalanche photodiode, is used to capture the transmitted or reflected light from the cavity. The detector should have high sensitivity and fast response to capture the ring-down signal accurately.

The detector output is typically connected to a data acquisition system, which records the ring-down signals and converts them into digital data. The data can be processed using various signal processing techniques, such as Fourier transform analysis or exponential fitting algorithms, to extract the ring-down time and calculate the target gas concentration.

It's important to note that the specific instrumentation and approaches can vary depending on the CRDS system manufacturer, the target gas, and the application requirements. CRDS can achieve extremely high sensitivity, allowing for detecting and measuring trace amounts of gases, even at parts per billion (ppb) or parts per trillion (ppt) levels. The absorption spectrum of the target gas can be precisely matched using a tunable laser, providing excellent selectivity against interference from other gases. CRDS provides rapid measurements, enabling real-time monitoring of trace gases. CRDS has been successfully applied in various fields, including environmental monitoring, atmospheric science, industrial process control, and medical diagnostics [56].

2.2.3 Mode Matching

In order to efficiently couple the incoming light to the cavity, the laser beam should be properly "mode matched" meaning that the beam's geometric properties (waist size and location) should be matched to those required by the optical cavity theory (typically based on the fundamental TEM_{00} mode of the laser). The characteristics of a Gaussian beam can be fully described by the radius of curvature, R, and the beam waist, w at a specific position, z.

The beam radius, w(z), can be determined using the equations:

$$w(z) = w\sqrt{1 + \left(\frac{z}{z_R}\right)^2} \tag{8}$$

$$R(z) = z\left[1 + \left(\frac{z_R}{z}\right)^2\right] \tag{9}$$

$$z_r = \frac{\pi\omega_0^2}{\lambda} \tag{10}$$

Where ω_0 represents the beam waist, and z_r is the Rayleigh range, which denotes the distance over which the beam remains within $\sqrt{2}$ times the beam waist.

The mode matching of the laser beam (to the cavity) involves matching the Gaussian properties of the beam with those of the optical cavity. Typically, lenses are employed to shape the laser beam externally, ensuring its conformity to the cavity when it passes through the cavity-entrance mirror. By precisely overlapping the beam with the cavity, the beam effectively couples spatially to the cavity. Then, to effectively inject light into the cavity, one must also frequency match the laser to the cavity. The frequency matching is done by scanning the frequency (wavelength) of the laser with resonance established whenever the cavity length is an integer multiple of half the laser wavelength. This condition also corresponds to matching the laser frequency to an integer multiple of the cavity's free spectral range (FSR):

$$FSR = \frac{\mathrm{c}}{2\mathrm{nL}} \tag{11}$$

were, n represents the refractive index of the material within the cavity (often one has n=1 for air).

2.2.4 Details of Continuous Wave CRDS

Continuous Wave Cavity Ring-Down Spectroscopy (CW-CRDS) is a variant of CRDS that employs continuous-wave (CW, or c-w) lasers to yield higher sensitivity detection (typically to measure lower concentrations than would otherwise not be possible). In this approach, a c-w laser beam is injected into the cavity, and the cavity is monitored for the rate of light decay. CRDS was initially only deployed with pulsed lasers but in 1996 Romanini et al. demonstrated the use of a c-w laser for CRDS [57],

[58] in a relatively simple and low-cost setup which paved the way for many future studies.

CW-CRDS relies on precise measurement of the decay time of the light within the cavity. The light decay is typically analyzed using sensitive detectors, such as photodiodes or avalanche photodiodes, which can detect very small changes in light intensity. The decay time is measured by analyzing the exponential decrease in light intensity after the laser is extinguished with an acousto-optic modulator (AOM) tied to a trigger circuit (that monitors the light level injected to the cavity). The AOM itself works through the acousto-optic effect, where the interaction of sound waves and light waves leads to changes in the optical properties of the material (Figure 6).

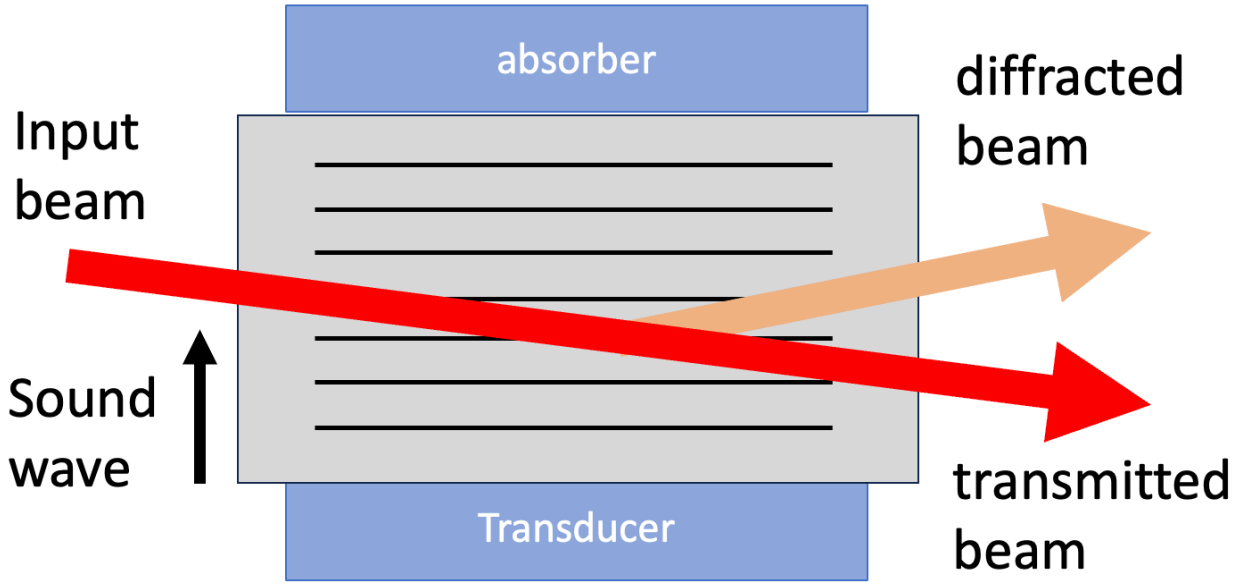

Figure 6: Basic operation of an acousto-optic modulator [59].

CW-CRDS finds applications in various fields, including environmental monitoring, atmospheric science, combustion research, and trace gas analysis. The method is used to study greenhouse gases, air pollutants, and volatile organic compounds. The technique also enables the detection and quantification of isotopic ratios, which can provide insights into chemical and biological processes. A specific

example of CW-CRDS for moisture detection is provided by Dudek et al [60]. A 1322 nm system with a mirror reflectivity of 99.985 % was used to detect moisture with a lower detection limit of 3 ppbv. Trace moisture detection is another critical measurement for cleanrooms, especially in semiconductor manufacturing.

2.3 Characterization of Detection Limit

CRDS detection limits can be examined using Allan variance methods [61]. The Allan variance is a statistical measure commonly used to assess the stability and noise characteristics of a measurement system such as CW-CRDS. The Allan variance data provides information about the precision and repeatability of the measurement over different time intervals. By analyzing the Allan variance, one can determine the detection limit of the CW-CRDS system, in terms of minimum detectable concentration, as a function of measurement duration. Note that the term lower detection limit (LDL) is often used interchangeably to describe the detection limit.

The Allan variance is typically calculated by performing repeated measurements at varying integration times and analyzing the resulting data. The Allan deviation (σ) is the square root of the Allan variance and represents the standard deviation of the measurement as a function of the integration time.

Figure 7 shows an example Allan variance plot generated from methane concentration readings over time [61]. It shows an Allan variance of ~ 9 ppb at one second with the most optimal integration time of 200 seconds with an Allan variance of ~ 1.5 ppb.

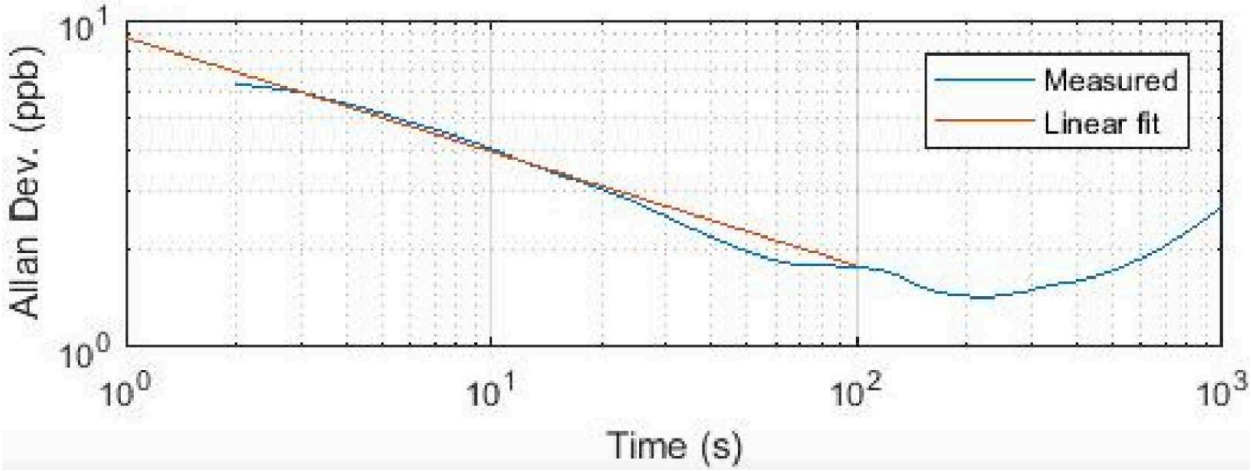

Figure 7: Allan deviation as a function of time for methane detection with a CRDS system [61].

2.4 Past Work on HCl CRDS

The current CRDS setup borrowed a lot of its equipment and setup details from earlier work done by Professor Yalin's group in connection with detecting HCl in the atmosphere [45]. The setup employed a distributed-feedback (DBF) diode laser at 1742 nm wavelength in conjunction with a high finesse 90 cm cavity. This setup accurately and quantitatively measured the concentration of HCl allowing the detection of HCl concentrations as low as <20 parts per trillion by volume (pptv) within a minute. Additionally, the instrument demonstrated a rapid response time of less than 15 seconds when detecting changes in the input HCl concentration. It should be noted that the earlier system used a closed-path where the cavity pressure was controlled to a fraction of an atmosphere, whereas in the present cleanroom configuration we desire the system to operate open-path (with no flow system and with the sample gas at ambient conditions).

In other work, Hildén Panu et al. utilized a CRDS analyzer based on a diode laser operating at 1742 nm and a bismuth-doped fiber amplifier to detect HCl in cleanroom environments [62]. They specifically studied the sources of potential HCl

leaks in a cleanroom to conduct their experiments. Their instrument resulted in LDL of 3.06 ppb with an integration time of 60 seconds and a standard deviation of 0.98 ppb [62]. Wilkerson et all have demonstrated the detection of stratospheric HCl using three mirrors integrated cavity output spectroscopy that utilized a CW interband cascade laser centered 3.37 μm [63]. The approach is very similar to CRDS except that the instrument is fitted with a third mirror called a reinjection mirror (RIM), which propagates more light in the cavity resulting in more light being delivered to the detector. The RIM is placed before the laser enters the cavity through the first mirror which allows for the majority of the light that is reflected in from the first mirror to be “reinjected” into the cavity resulting in more light on the detector. The instrument had a 30 s precision of 26 pptv.

None of the aforementioned CRDS HCl instruments have been specifically designed for cleanroom integration. Although their LDL is well below SEC’s cleanroom requirements, their bulky size renders them undesirable for cleanroom applications. Our work aims to fulfill the size and weight requirements for SEC's mobile platform while concurrently meeting LDL standards for cleanroom environments. Furthermore, none of these instruments has been used for simultaneous particle counting (along with AMC detection) as we seek to develop.

2.5 Particle Detection by CRDS

2.5.1 Theory of Mie Scattering

Mie scattering, named after Gustav Mie, provides a mathematical framework for describing the scattering of electromagnetic waves by spherical particles. It is widely used to understand and analyze the interaction of light with particles of various sizes,

such as droplets, aerosols, and solid particles. The theory assumes that the incident light interacts with the particle, causing it to oscillate and re-radiate electromagnetic waves. These scattered waves interfere with the incident wave, resulting in a complex pattern of scattering characterized by intensity, direction, and polarization [14].

Mie scattering applies when scattering particles are comparable in size to or larger than the wavelength of the incident radiation. In contrast, Rayleigh scattering occurs when particles are much smaller than the wavelength of the incident light. For visible light, the angular distribution of scattered light for particles larger than approximately 0.05 μm requires the use of the Mie equations. Mie scattering theory offers a comprehensive solution to the problem of light scattering by spheres, accommodating both absorbing and non-absorbing spheres ranging from molecular sizes to particles that can be analyzed using classical optics [14], [64].

The Mie solution represents the complete formal solution of Maxwell's equations, encompassing the vector wave equations for the incident wave, the wave within the particle, and the scattered wave with a set of boundary conditions at the particle's surface. A detailed derivation of this theory and an explanation of the equations can be found in van de Hulst's work from 1957 [65] and Kerker's book [66].

A single Mie solution can be obtained for one value of the particle refractive index (real and imaginary), size parameter (α), and the scattering angle (θ). The sizing parameter (α) is given by:

$$\alpha = \frac{\pi d}{\lambda} \tag{11}$$

where d is the diameter of the particle and λ is the wavelength of light interacting with it.

The scattered intensity at a distance R and direction θ from a spherical particle illuminated with an unpolarized light of intensity of I_0 is:

$$I(\theta) = \frac{I_0 \lambda^2 (i_1 + i_2)}{8\pi^2 R^2} \quad (12)$$

where i_1 and i_2 are the Mie intensity parameters (calculated from Mie theory) for scattered light with perpendicular and parallel polarization, respectively.

An example of the Mie intensity parameters for water droplets with different size parameters is provided in Figure 8.

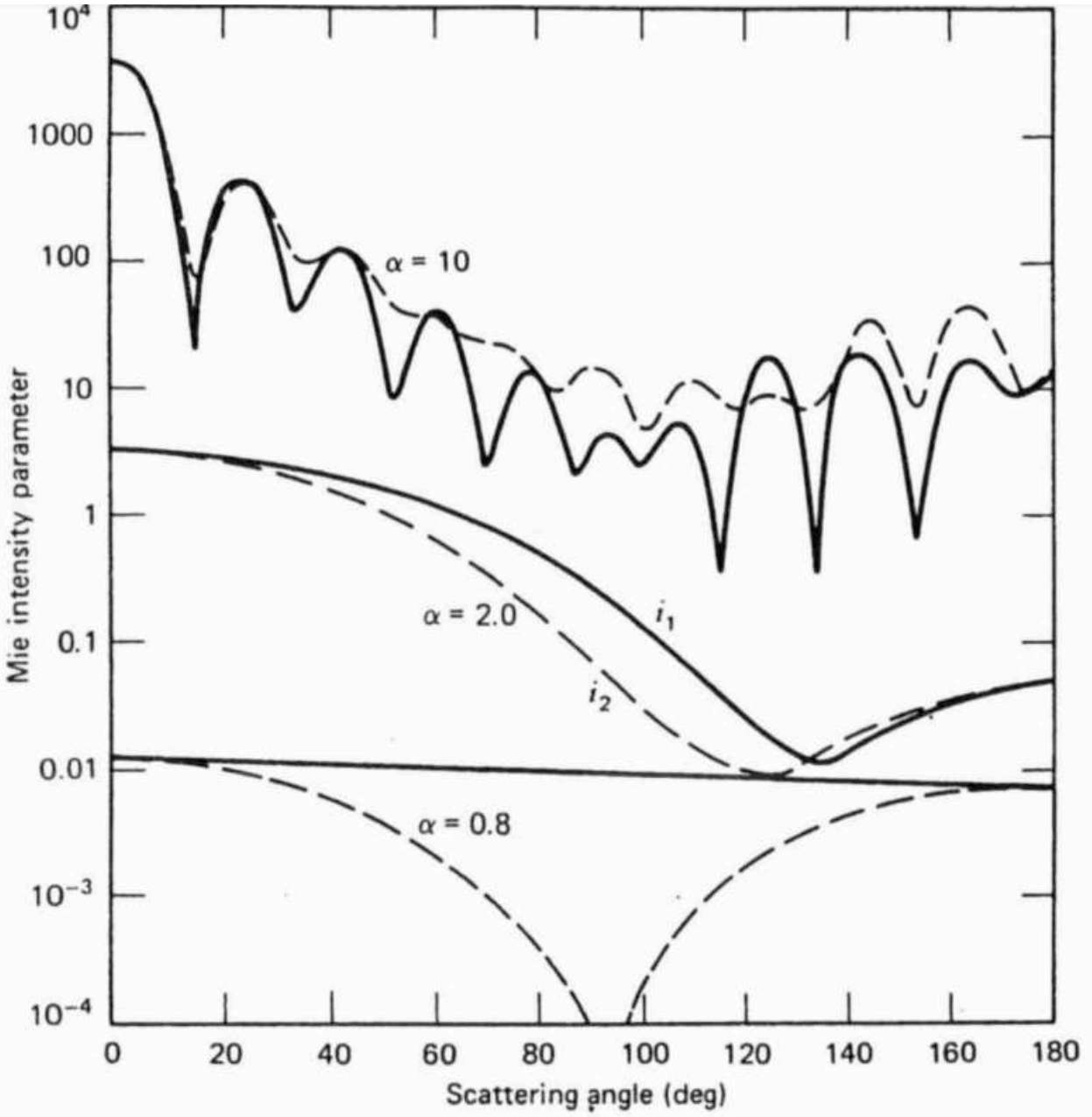

Figure 8. Mie intensity parameters versus scattering angle for water droplets. Solid lines are $\boldsymbol{i_1}$ and dashed lines are $\boldsymbol{i_2}$ [14].

The relative scattering (total scattering) depends strongly on the size parameter. This relation is highlighted in Figure 9 where the combined Mie intensity parameter for water droplets as a function of the particle size parameter for scattering at θ = 30° and 90° are shown.

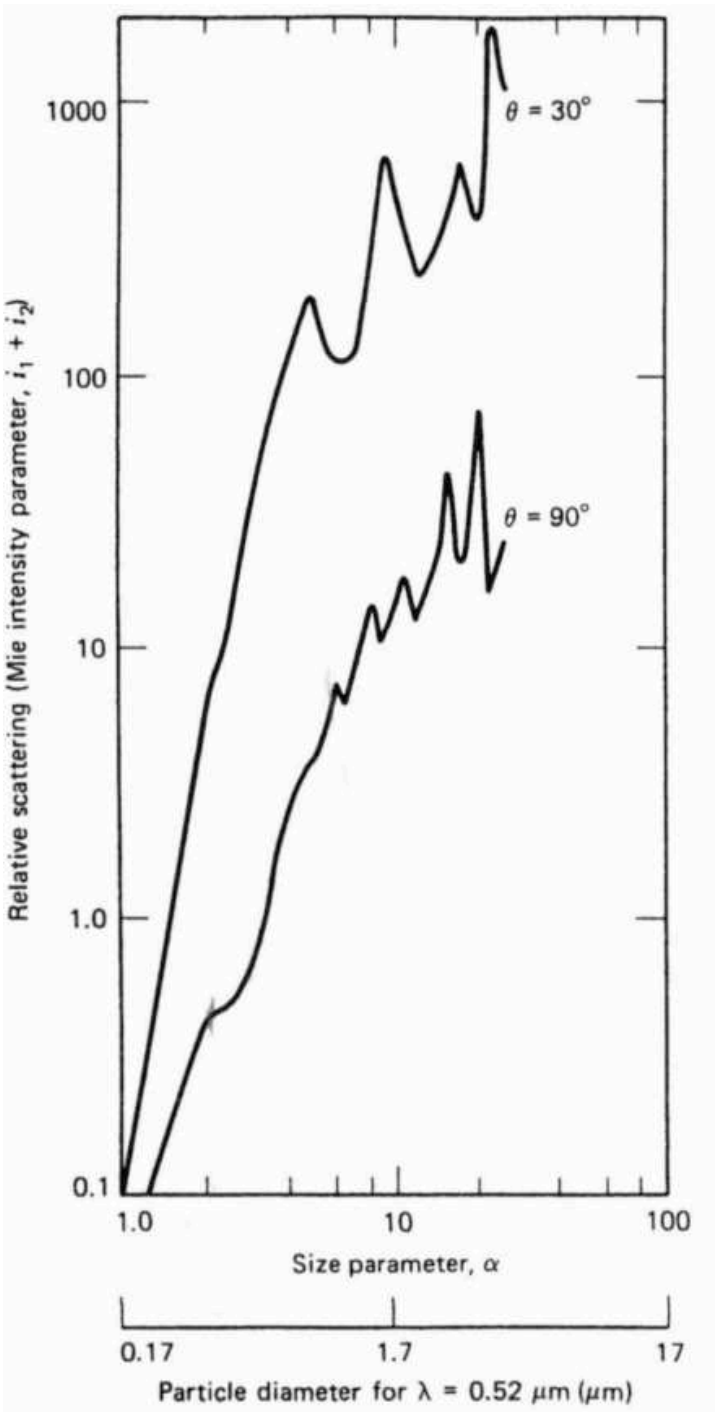

Figure 9. Relative scattering [Mie intensity parameter $(\boldsymbol{i_1 + i_2})$] versus size parameter for water droplets at scattering angle of 30° and 90° [14].

The application of Mie scattering theory spans various scientific and technological domains. In atmospheric science, Mie scattering plays a crucial role in understanding the interaction of sunlight with aerosol particles, providing insights into

the formation of clouds, climate modeling, and air quality monitoring [67]. Mie scattering is utilized in optics to analyze and design optical components, such as anti-reflective coatings and diffusers [68]. It is also employed in the field of remote sensing to interpret the scattering properties of Earth's surfaces and study the composition of atmospheric particles. Additionally, Mie scattering finds applications in nanotechnology, where it aids in characterizing and manipulating nanoparticles, enabling advancements in fields like nanoparticle synthesis, drug delivery, and nanoscale imaging [69]. With its versatility and wide-ranging applications, Mie scattering theory continues to contribute significantly to our understanding of light-matter interactions and pave the way for technological advancements in various disciplines.

2.5.2 Past work on Particle Detection by CRDS

Past work done in our lab has shown shorter (and fluctuating) ring-down times due to the increased optical extinction associated with the Mie scattering. Figure 10 shows increased noise in the presence of particles from ambient laboratory air. The long tail at higher absorption values is also indicative of additional scattering loss due to particles. In that earlier work, these ring-down fluctuations were considered as a noise source that reduced the sensitivity for target gas detection [70]. The current research takes a different approach in that we seek to analyze the fluctuations in ring-down time to gain information on particle quantification.

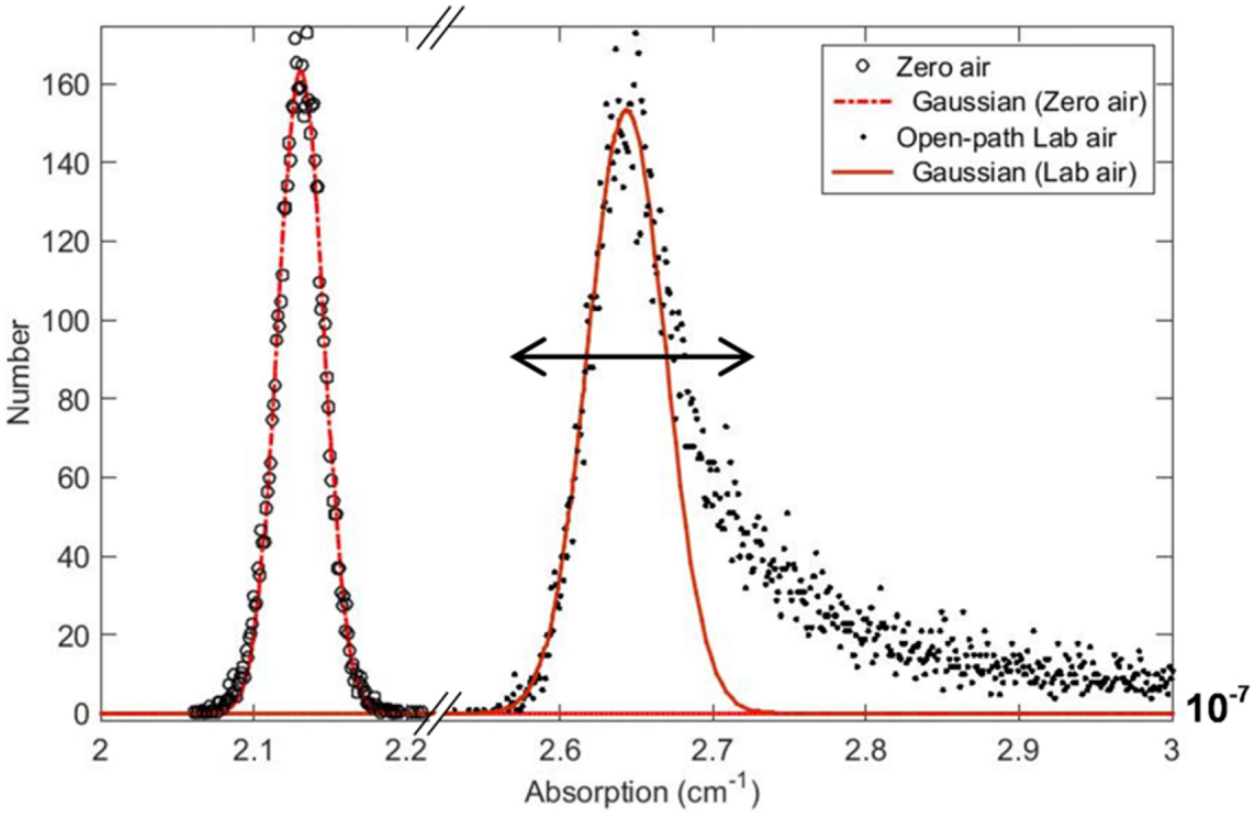

Figure 10: Histogram of CRDS absorption measurements for closed cell measurement of zero air with no particles (left) and open-path measurement of ambient laboratory air (right) [70].

Previous research on particle detection by CRDS has demonstrated its effectiveness and versatility in various applications. One study focused on the retrieval of optical properties of absorbing and non-absorbing particles with CRDS [71]. Multiple pure and mixed aerosols were generated in the lab to conduct this study. The researchers successfully measured the extinction coefficient, extinction cross-section, and extinction efficiency for the particles generated. The refractive indices of various aerosols were determined by comparing the measured extinction efficiency of each aerosol variant with the extinction values predicted using Mie theory. Another study explored the application of CRDS for the precise retrieval of the refractive index for a single particle in an optical cavity [72]. By fitting experimental measurements to Mie

calculations, which were adjusted to consider the presence of an intracavity standing wave, the refractive index of 1,2,6-hexanetriol particles (at relative humidity levels below 10%) was accurately determined as 1.47824 ± 0.00072.

Gordon et al. have demonstrated the use of open-path CW-CRDS utilizing a multimode continuous-wave diode laser centered at 674.22 nm to measure extinction coefficients of aerosols [73]. There 1σ detection limit for one second of averaged data was 0.05 Mm^{-1}. The open-path system had no inlet tubing, allowing for the minimization of particle losses due to impaction. For shorter averaging times (< 1s) the open-path cavity performs better than closed-path because in open-path aerosol travels perpendicular to the beam, resulting in shorter residence time and hence leading to less successive laser shots being correlated (Figure 11) [73].

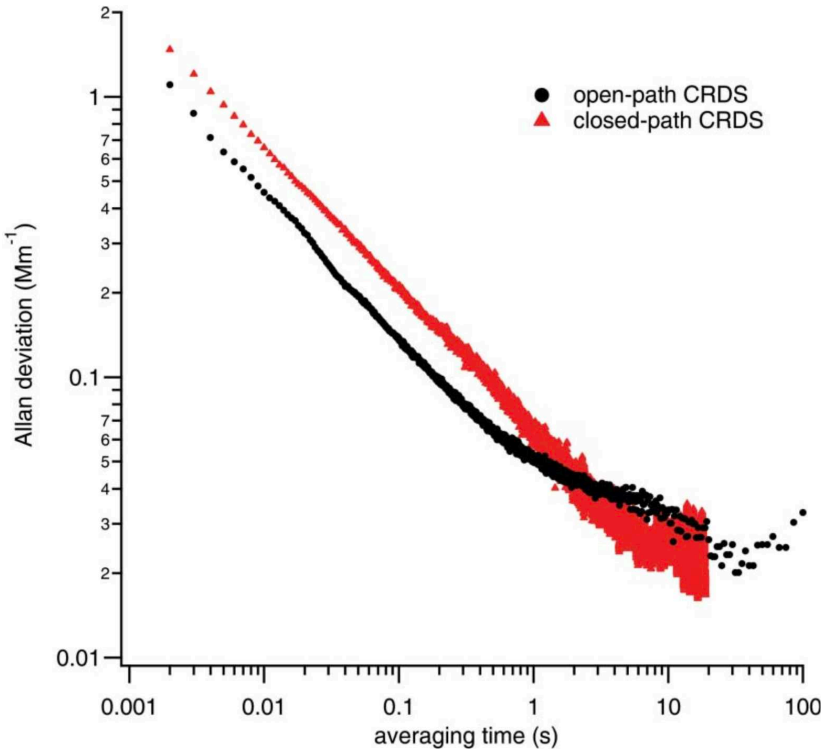

Figure 11. Allan deviation of extinction coefficient in zero air for the Open-path CRDS and conventional closed-path CRDS. Both systems are stable (minimum deviation) and converge to similar minimum detection limits when ring-downs are averaged for up to 20 s. The closed-path CRDS trace (red triangles) is from Langridge et al [73], [74].

These approaches show some capabilities of obtaining various information from light-particle interaction but, to the best of our knowledge, no one has attempted to quantify particle concentrations using CRDS. Furthermore, streamlining a compact mobile system for simultaneous HCl and particle detection with a focus on cleanroom implementation is novel relative to past research.

CHAPTER 3: Design and Development of Open-Path CRDS for Cleanroom Detection

3.1 Testbed Chamber for Setting Fixed HCl and Particle Levels

A testbed was developed to deliver and set controlled HCl and particle concentrations. This operated by maintaining a very slight vacuum in the sampling chamber, which ensured that the chamber was flushed with a constant flow of the desired mixture of air to be analyzed by CRDS. This is attained by connecting pumps at the inlet and outlet of the system. The air flow could not be stopped for the duration of a test because if the air flow stopped, the chamber air would mix with ambient air. The HCl line was mixed with clean air in different proportions to attain different concentration values. The clean HEPA-filtered air was mixed with dirty air to deliver different particle concentrations.

A schematic of this setup is provided in Figure 12. Ambient lab air was pulled with a pump (Gast 86R123-101-N170X) through a pressure regulator (Fairchild model 30232) to maintain a steady flow of 22 L/min air as the pump can produce significant variations in the flow rate (when used without a regulator). This stable flow was then divided into two lines individually administered by a control needle valve. The first line was passed through a HEPA filter (PALL 12144) which removed 99.99% of particles equal to or greater than 0.3 μm in size. The second line is passed through a rotameter (Dwyer RMA-151-SSV) for more precise control of the dirty ambient air flowing in and to monitor the flow rate of dirty air going in. These two lines are then joined again before passing into the control chamber. By alternating the flow rates using the control valves

on these two lines, air of different ISO levels can be delivered into the control chamber. The flow rates would be adjusted until the desired particle concentration was observed on the CPC (TSI Condensation Particle Counter 3787). A third line attached to a 1 ppm HCl cylinder (balance of gas is air) is also connected for HCl testing. A cylinder regulator (CGA 330) is used to deliver HCl in this line and significantly higher air flow is propagated for HCl tests so as to substantially dilute the HCl line (e.g., by a factor of 100 to achieve a concentration of 10 ppb). This method allows for variable dilution while maintaining the enclosure at near atmospheric conditions. For HCl tests, the chamber is run at a very slight vacuum i.e., a vacuum pressure of 0.05 inches of water to reduce risks of fugitive HCl escaping the enclosure. The inlet and outlet legs need to be balanced to maintain this vacuum, which is achieved using the needle control valve on the inlet and outlet lines. To monitor this vacuum, the chamber is attached to a differential pressure gauge (Magnehelic 2000-00N). The chamber air is finally let out through a control valve which is connected to a pump (Varian IDP2B01) pushing this air into the exhaust. Note that the balancing of inlet and outlet lines (to create slight vacuum) is only important for HCl tests so as to not leak the harmful HCl gas in the lab. Particle tests can be performed under positive pressure without any need for the outlet being connected to an exhaust. The control chamber is a 90 cm x 60 cm x 30 cm airtight acrylic box. The chamber houses the CRDS optoelectronics which are externally supplied by cabling that runs through the chamber wall through a sealed feedthrough.

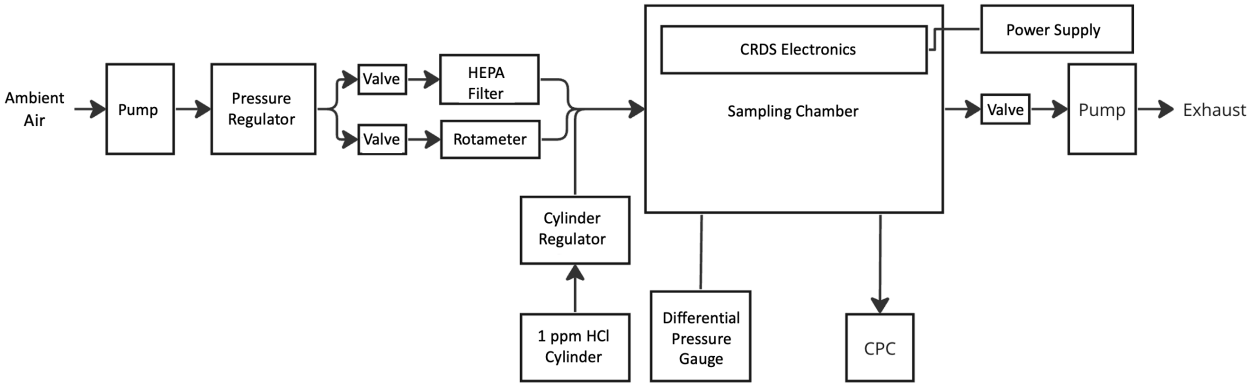

Figure 12. Schematic of the delivery system and control chamber.

The chamber is capable of attaining ISO 5 level within approximately 45 minutes after starting from ambient lab air (ISO 10 or greater). It takes another 45 minutes to bring the chamber to ISO 3 level.

3.2 Laser Sensor Optoelectronics

The design of our CRDS setup borrows heavily from previous work conducted at this lab [45], [61]. The main reason for this was to extrapolate existing work with modifications to allow us to meet the objectives of the cleanroom sampling project quickly.

As will be shown below with spectral simulations we operate the CRDS sensor in the region of 1742 nm in the near-infrared (NIR). Despite our selected wavelength of 1742 nm falling slightly outside the standard telecommunications bands, most of the required equipment (laser, fiber optics, mirrors, etc.) is readily available from telecom suppliers. In contrast, another possible wavelength would be 3.4 μm to access the (stronger) fundamental (1-0) vibrational band of HCl; however, this region has less availability of components and requires, for example, a lead salt laser, difference-frequency generation (DFG) laser sources (Weibring et al., 2010) [75], or interband

cascade lasers. However, these sources and their associated components tend to be more expensive and less developed in commercial applications.

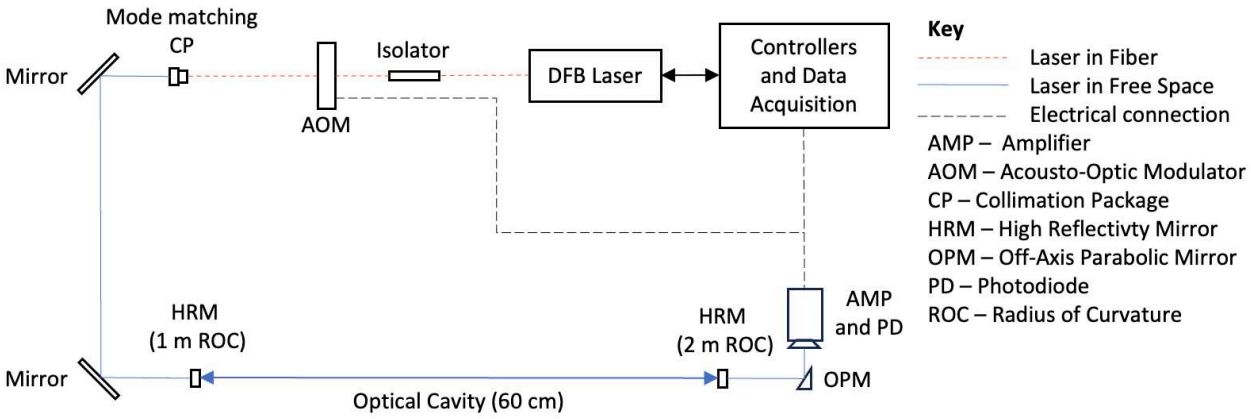

Figure 13: Optical components and data acquisition system of the CRDS sensor.

Shown in Figure 13 schematic of the optical components and data acquisition system used for our CRDS system. We utilize a distributed-feedback diode laser in a 14-pin butterfly package (KELD1F5DAAA, NEL Lasers) with specific characteristics, including a center wavelength of 1742 nm, linewidth of a few MHz, and 15 mW of output power through a single-mode fiber pigtail. To maintain precise control, a Thermo-electric cooler (TEC) affixed to the diode regulates the laser temperature, ensuring the stability of the center of the overall scan region. This enables current-scanning of the laser, facilitating the recording of the spectrum. The laser beam initially traverses an acoustic-optic modulator (Brimrose, 1801-SY-16708) functioning as an optical switch. When the data acquisition (DAQ) system (see below for details on the processor) detects resonance within the optical cavity, the computer triggers the shutdown of the acousto-optic modulator (AOM), initiating a rapid extinction of the incoming laser beam, with a time constant of approximately 300 ns [45]. Subsequently, the laser beam passes

through an aspheric collimation lens (Thorlabs, CFC-11X-C, focal length = 11 mm) for mode-matching to the cavity. Precisely positioning this aspheric collimation lens relative to the fiber output is essential to achieve spatial mode matching, specifically aligning the beam with the $TEM_{0,0}$ mode of the cavity. This positioning also necessitates the correct separation distance between the cavity and the lens (~ 22.6 cm). After exiting the lens, the laser beam proceeds through free space and is then directed by two steering mirrors into the optical cavity. The optical cavity itself consists of two high-reflectivity dielectric mirrors (Advanced Thin Films), featuring radii of curvature (on the inner side of the cavity) measuring 1 m where the light enters cavity and 2 m on the side of the photodetector, with a separation distance of 60 cm between them. The chosen radii were selected to minimize the necessary mode-match distance. A mirror reflectivity of R=99.9981% was assessed by obtaining an empty-cavity ring-down time of 105 μs, aligning closely with the manufacturer's specifications. To detect light in the near-infrared (NIR) range, an extended wavelength InGaAs photodiode (G8421-03, Hamamatsu) is employed, connected to a transimpedance amplifier (341-4-inv-10PF, Analog Modules). This amplifier has gain adjusted to 2×10^6 V/A and a bandwidth of 2 MHz, ensuring that the ring-down signals were accurately captured without distortion. The bandwidth is approximately 5 times larger than needed in order to not distort the ring-down signals [45]. Using a detector with a higher bandwidth than required results in increased noise, as high-frequency detector dark noise is unnecessarily amplified.

A core electronics platform is established through the integration of a tailored carrier board with a sbRIO-9651 system, based on the Xilinx Zynq-7020 system on chip (SoC). This configuration served the purpose of detecting and processing analog

signals originating from the photodetector. These signals at mode match conditions would peak at about 1 V. A sample ring-down signal is shown in Figure 14.

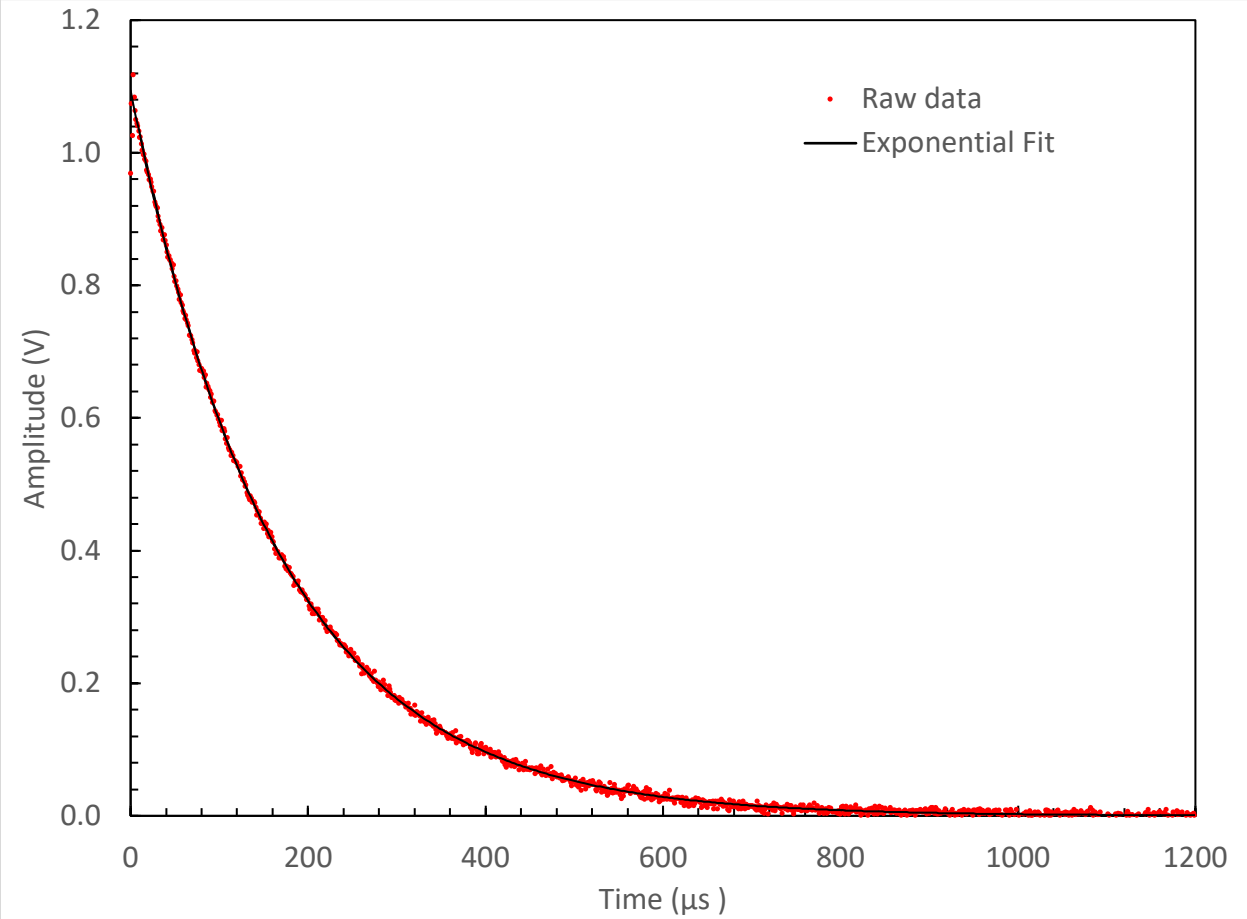

Figure 14: A sample ring-down with time in µs. Red trace is raw data while the black curve is exponential fit.

A specialized LabVIEW program (developed by TCB Engineering) is employed to manage the instrument and oversee data acquisition and processing. Initially, the software dispatches an analog voltage to the laser controller, causing the laser to traverse a triangular waveform between 5739.00 and 5739.50 cm^{-1}, completing one cycle in 1 second. This analog output stems from a 16-bit digital signal, resulting in 520 discrete wavelength points across the scanning range. The software monitors the photodetector signal emanating from the cavity. When this signal surpasses a

predetermined threshold, indicating that the laser is in resonance with the cavity, the LabVIEW software deactivates the AOM, digitizes the ring-down signal, and applies an iterative nonlinear least squares fitting method initiated by a linear least-squares fit to the acquired data. Every time a ring-down event is detected, the relative laser frequency is computed using the etalon calibration. The entire data acquisition (DAQ) system has the capacity to capture over 200 ring-down events per second, which exceeds the necessary speed, given that the system's optical limitations restrict it to around 20 triggers per second. Raising the laser scan speed, and consequently the acquisition rate, reduces in the light passing through the cavity, thereby diminishing the overall sensitivity of detection. After determining the ring-down time, it is then converted into the absorption coefficient, denoted μ, which continues to encompass the loss associated with an empty cavity (eqn. (7)).

In some cases, particularly for ring-down data collection for particles (as opposed to HCl), a slightly different setup was used. In this case, the cavity detector voltage signal was digitized by a 2.5 MS s^{-1}, 14-bit PCI multi-purpose DAQ card (PCI-6132, National Instruments, Austin, TX, USA), which also controlled the AOM. This was done because sbRIO-9651 showed slightly more noise in acquiring and fitting ring-down times, which negatively affected the ability to infer particle densities from ring-down fluctuations.

The complete acrylic chamber with all optoelectronics inside of it can be seen in Figure 15.

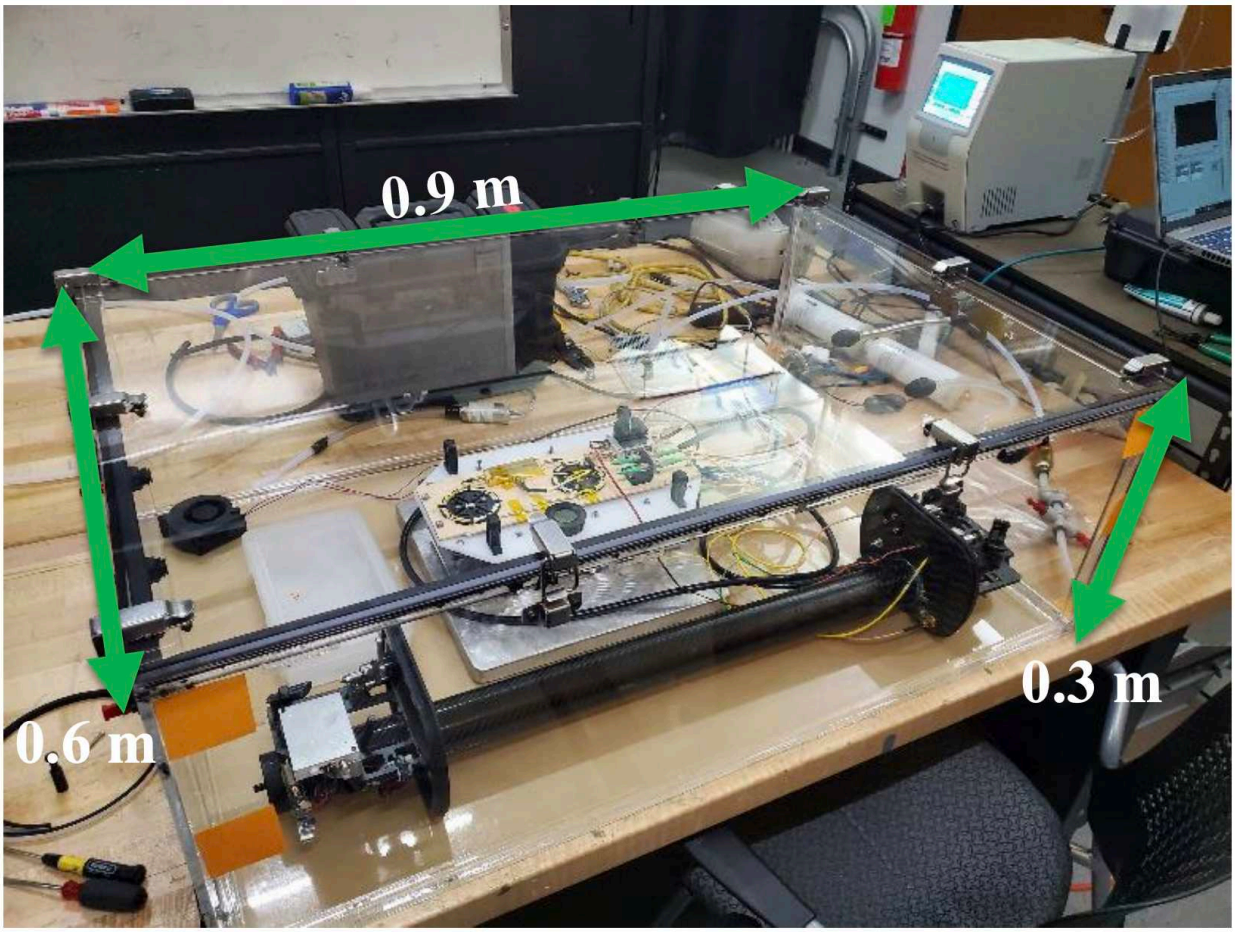

Figure 15: Chamber with CRDS equipment.

3.3 Scan Region and Spectral Fitting for HCl Measurements

The design of a spectroscopic instrument for absorption measurements is determined by the characteristics of the targeted absorption feature(s), specifically its location and strength. In our instrument, we opted for the R(3) $H^{35}Cl$ line within the (2-0) absorption band (refer to Figure 16, Rothman et al., 2013) [76] due to several advantageous attributes. This choice was influenced by its relatively strong linestrength, distinct separation from other atmospheric absorbers, and compatibility with available near-infrared (NIR) components. The (2-0) band corresponds to molecular transitions from the initial vibrational level v'' = 0 (vibrational ground state) to the final level v' = 2 as a photon is absorbed. In Figure 16, we identify the first 5 P- and R- branch transitions

(absorption lines). Each transition consists of two closely situated lines, representing absorption by the two isotopologues $H^{35}Cl$ and $H^{37}Cl$. The measured concentrations account for isotopic abundances (0.758 for $H^{35}Cl$ and 0.242 for $H^{37}Cl$), providing information about the overall HCl population, encompassing both isotopologues. This specific absorption line has also been adopted by other researchers for laser absorption measurements of HCl (Panu et al., 2021; Ortwein et al., 2010)[62], [77].

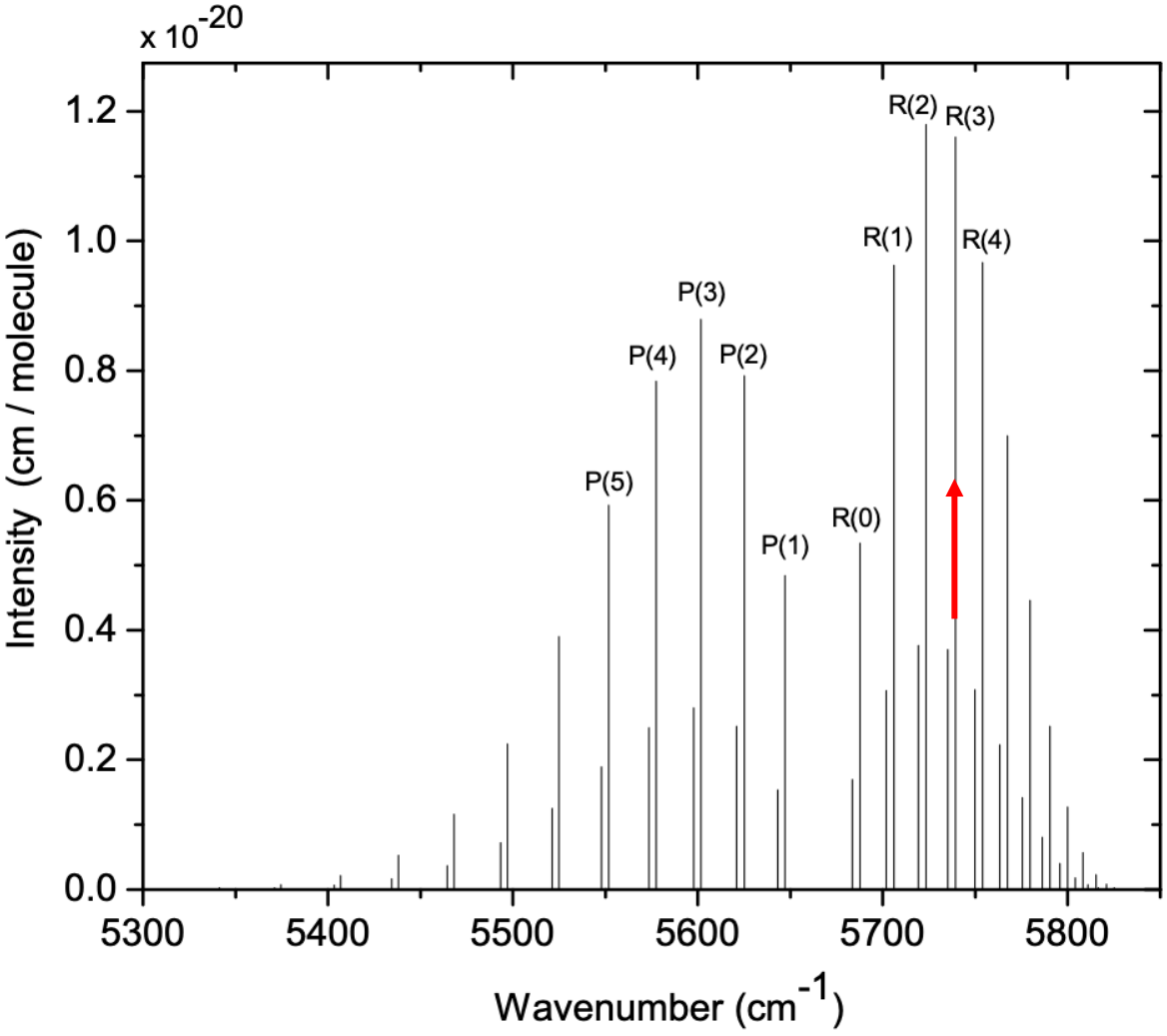

Figure 16. Line strengths of rotational lines of the 2-0 vibrational absorption band of $H^{35}Cl$ and $H^{37}Cl$ from HITRAN. The CRDS sensor uses the R(3) line of $H^{35}Cl$ at 5739.26 cm^{-1} (indicated with red arrow) [45].

It is crucial to achieve separation from the absorption lines of other potential interfering molecules to ensure the success of optical measurements. We have considered potential interferences arising from anticipated ambient molecules and their corresponding isotopologues, including CH_4, CO, CO_2, HCl, H_2O, NO, and N_2O (at typical atmospheric concentrations). Figure 17 shows HCl simulation along with other molecules (from the above list) with absorption features in the nearby vicinity. Noticeably, water vapor does lead to an overall increase in absorption spectra of these peaks (as shown in Figure 17) but the HCl absorption feature is still present and detectable even in the presence of 10,000 ppm (1%) water vapor.

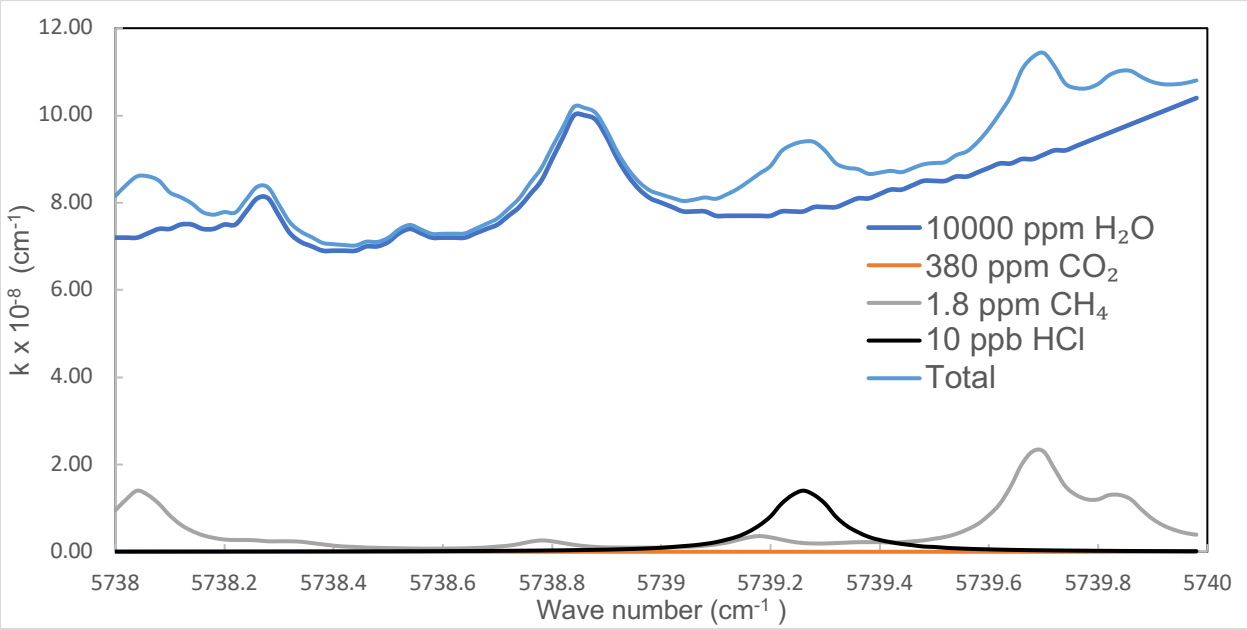

Figure 17: Simulated absorption spectra with 10 ppb HCl, 10000 ppm H_2O, 1.8 ppm CH_4 and 380 ppm CO_2 at 1 atm and 296 K.

The experiments on particle detection do not use resonant features and so we shorten and shift the laser scan parameters to a relatively flatter region (~5738.60 - 5738.65 cm^{-1}) to obtain these deviations and quantify them using standard moments.

Shown in Figure 18 is a simulation of the HCl peak at 108 ppb concentration in the region where our detection and analysis were made.

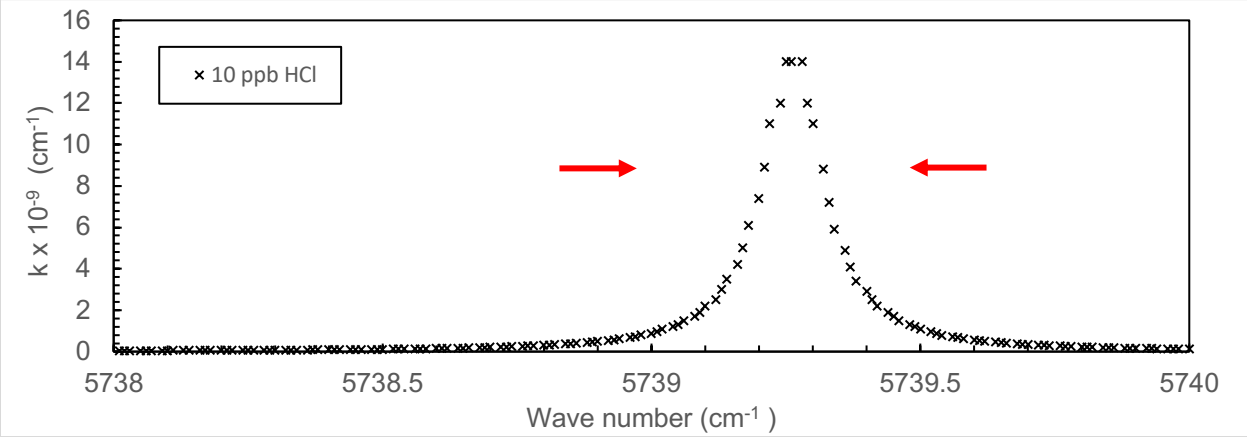

Figure 18: HCl analysis scan region (red arrows) with wave numbers on the x-axis.

A custom LabVIEW MathScript code was used to generate fittings for HCl measurements. Multiple ring-down values over discrete wavelengths along the scan region are averaged to generate an absorption spectrum. The laser would be scanned in a triangular pattern from 5739 cm^{-1} to 5739.5 cm^{-1} corresponding to an input current scan of 81 mA to 91 mA, producing 20 ring-downs per second. Assuming constant temperature and pressure throughout a test, the area under the spectrum curve would be directly proportional to concentration. This area was then used to calculate HCl concentrations; absorption coefficient, μ, is calculated using equation 7. HCl tests were validated using an earlier iteration of a CRDS system with same equipment used in lab by Hagen et al and more information can be found in their publication [45].

3.4 Preparatory Work on Laser Scanning

Initial electronics tests were conducted on a tabletop setup (Figure 19). This was done to test the viability of the setup. There were a few minor changes in design compared to the final setup described above. A 90 cm cavity instead of a 60 cm cavity

was used. A laser diode controller (ILX lightwave LDC 3714C) was used to operate the laser. DAQ card (PCIe-6321, National Instruments) was used to generate the analog voltage signal to the laser controller. The cavity detector voltage signal was digitized using a versatile 14-bit PCI multi-purpose DAQ card (National Instruments, model PCI-6132, Austin, TX, USA) with a sampling rate of 2.5 MS s−1. This same DAQ card also oversaw the control of the AOM.

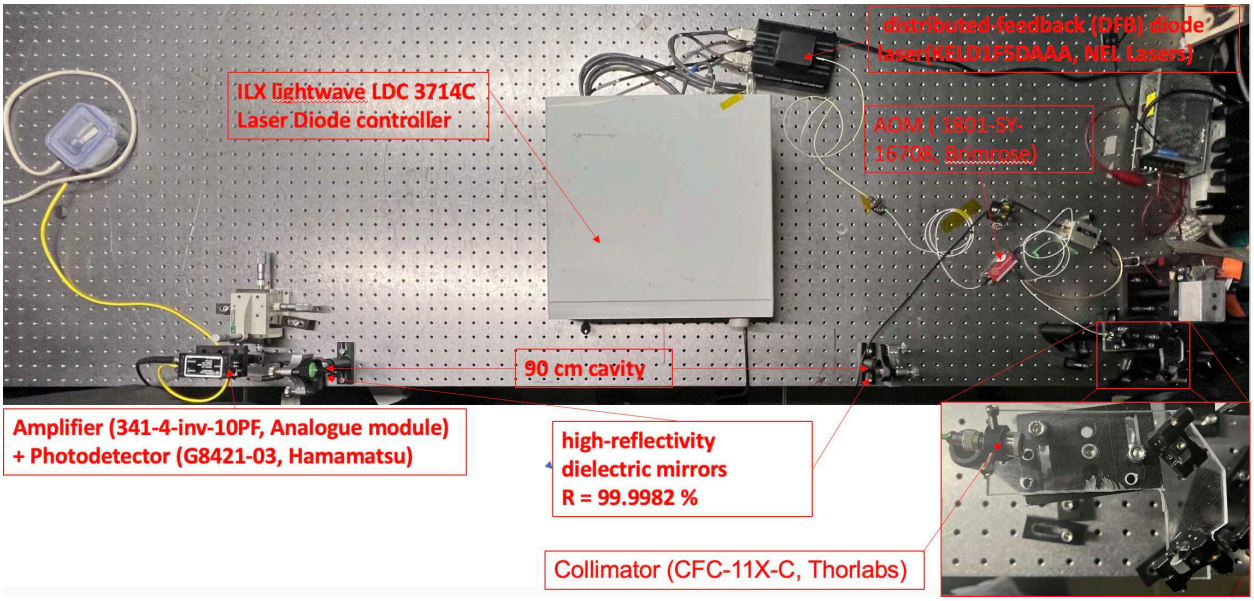

Figure 19: initial table-top setup of optoelectronics to test the scanning region of HCl.

We were able to obtain ring-downs with this setup, so the feasibility of this project was determined.

3.5 Analysis methods for Particle Detection

As discussed earlier, Mie scattering causes fluctuation in ring-down times and with lower PM concentrations we should obtain larger (mean) ring-down times indicative of less extinction within the cavity. For particle detection, we have considered different

approaches based on the variation in the distribution of ring-down times, including the use of standardized moments. These hypotheses are summarized below.

3.5.1 Analysis by Shifting of Mean of Ring-Down Time

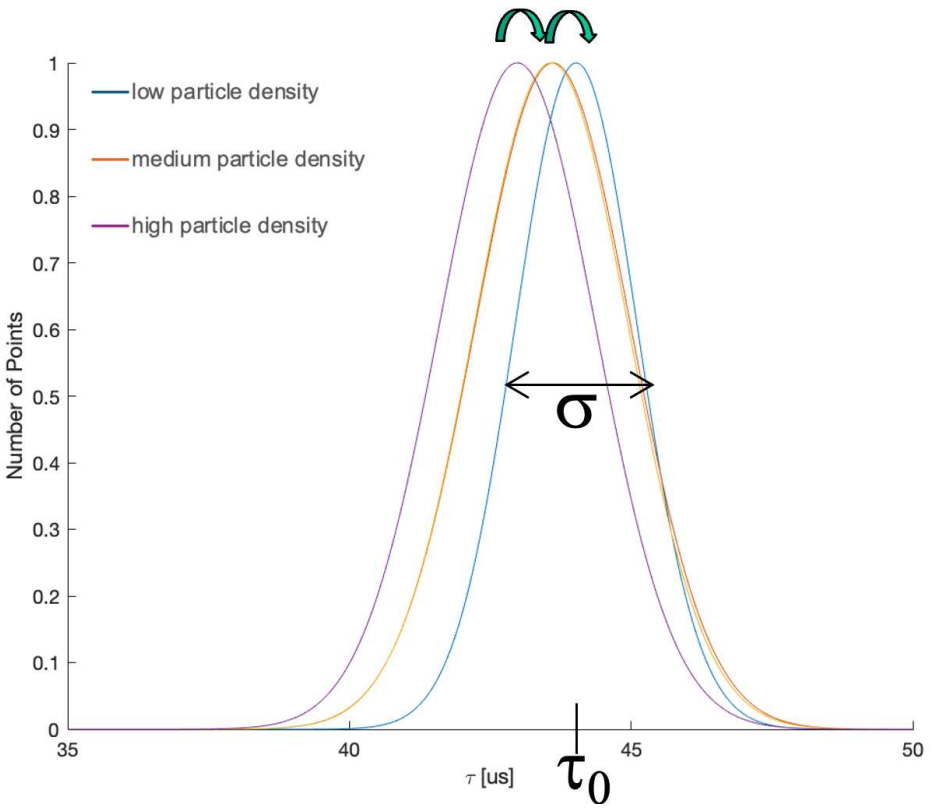

Figure 20: Simulated shifting of mean of distribution of ring-down times with different ISO levels.

Lower ISO levels would result in longer average ring-down times indicating less extinction. Less fluctuations in ring-down times due to less loss should also result in a narrower width. This hypothesis is shown in Figure 20.

3.5.2 Analysis by Outliers

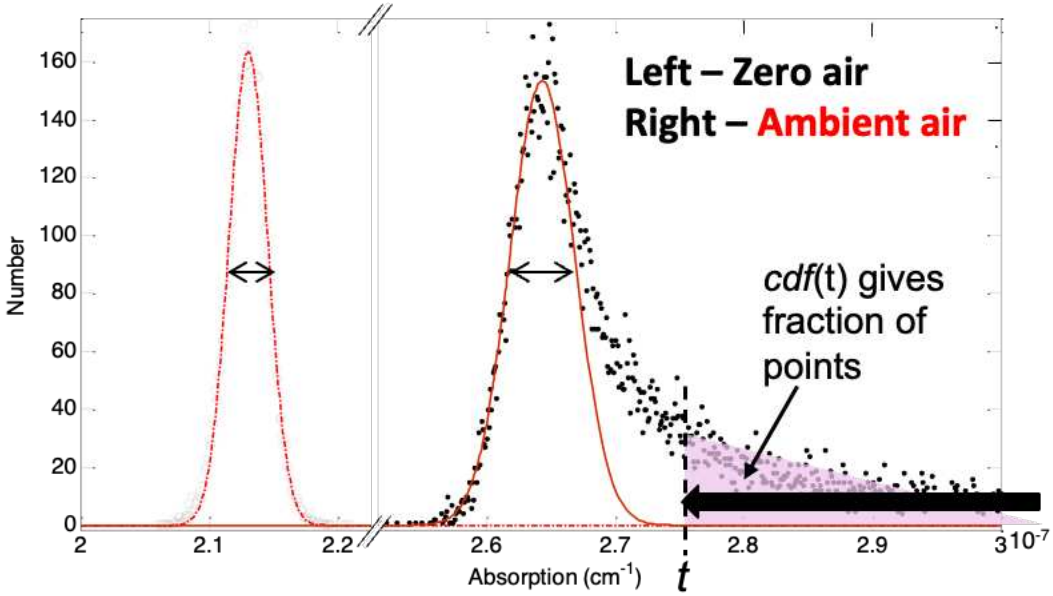

Figure 21: Example of outliers from a methane absorption spectrum [70].

The outliers in the ring-down signal due to additional loss for particles can be represented by a cumulative distribution function (cdf(t)). A fixed value of time, t, can be set to analyze the ring-downs outside of t. Figure 21 shows a spectrum with clean air (left) and a spectrum with dirty ambient air (right) that has an increased number of outliers from the ring-downs as a result of extra loss due to particle interaction. Note that cdf (outlier methods) have the advantage of being more self-referencing and less influenced by systematic drift. One way to quantify this is using the moments approach discussed later.

3.5.3 Analysis by Shape of Distribution – Analysis by Higher Order Moments

Moments are numerical quantities that describe various characteristics of a probability distribution or a set of data [78], [79]. The standard moment of a distribution is often used to measure the shape, central tendency, and spread of data. Moments allow for better understanding of the cdf.

For a distribution P(x), the (unnormalized) standard moment, γ_n, of degree *n* is found as:

$$\gamma_n = \int_{-\infty}^{\infty} (x - \gamma)^n \, P(x) dx \tag{13}$$

where γ_n is the mean (non-centralized first-moment). The centralized moments, of differing orders, carry different information. The centralized first-moment is, by definition, zero. The second central moment, also referred to as the variance, reflects the spread (width) of the distribution. The third central moment provides a measure of the skewness or asymmetry to the distribution. Finally, the fourth central moment provides a measure of the kurtosis, or "heavy-tail", of the distribution.

Overall hypothesis (A-C): Higher-order moments will reveal changes in distribution shape that are predictably influenced by particle concentration.

- 2nd moment corresponds to the variance or width of distribution.
  - **Hypothesis A:** Higher ISO will have a larger range of τ and therefore a higher 2nd moment (2nd moment taken about the centroid is basically the standard-deviation or FWHM of the distribution).
- 3rd moment relates to "skewness", i.e., asymmetry of the distribution (since, with the odd power, contributions from the "left/right" contribute differently).
  - **Hypothesis B:** Higher ISO will have a larger amplitude (negative) 3rd moment, due to more skewing to the side of low τ (hence negative).
- 4th moment relates to "kurtosis", i.e., the contribution of a "heavy-tail" to the distribution (since, with the high even power, contributions from "far" from the center are heavily weighted).

- **Hypothesis C:** Higher ISO will have a higher 4^{th} moment due to more of a heavy tail influence (outliers due to particles).

3.6 Sequential sampling

Sequential sampling was utilized for particle concentration calculations from the CPC. It is evident that at cleanroom conditions with lower ISO levels, we will have many triggers (ring-downs) that may not interact with any particles at all and hence will not have the required information for analysis. To overcome this issue, an approach derived from ISO 14644-1 (Annex D) is used [6]; sequential sampling allows for the use of longer integration times to infer the number of particles counted. This includes readings with zero particle counts.

Chapter 4: Results and Discussion

Here, we present and discuss the results of using our CRDS system for the detection of HCl and particles.

4.1 HCl detection

4.1.1 Data Examples

Multiple tests were conducted to understand the limitations of our cavity ring-down system. The delivery system was tested strenuously by delivering multiple concentrations of HCl. The standard deviation was about 1.2 ppb HCl in all our readings. The results from four of these tests conducted over 30 minutes of testing are shown below (Figure 22). Note that our controlled dilution scheme allowed rough, but not precise, setting of the delivered HCl concentration. The reported concentrations for the 4 curves in Figure 22 are due to the CRDS measurements themselves. However, this is deemed acceptable given that CRDS is self-referencing and our HCl CRDS detection scheme has been validated in past work (Hagen) [45].

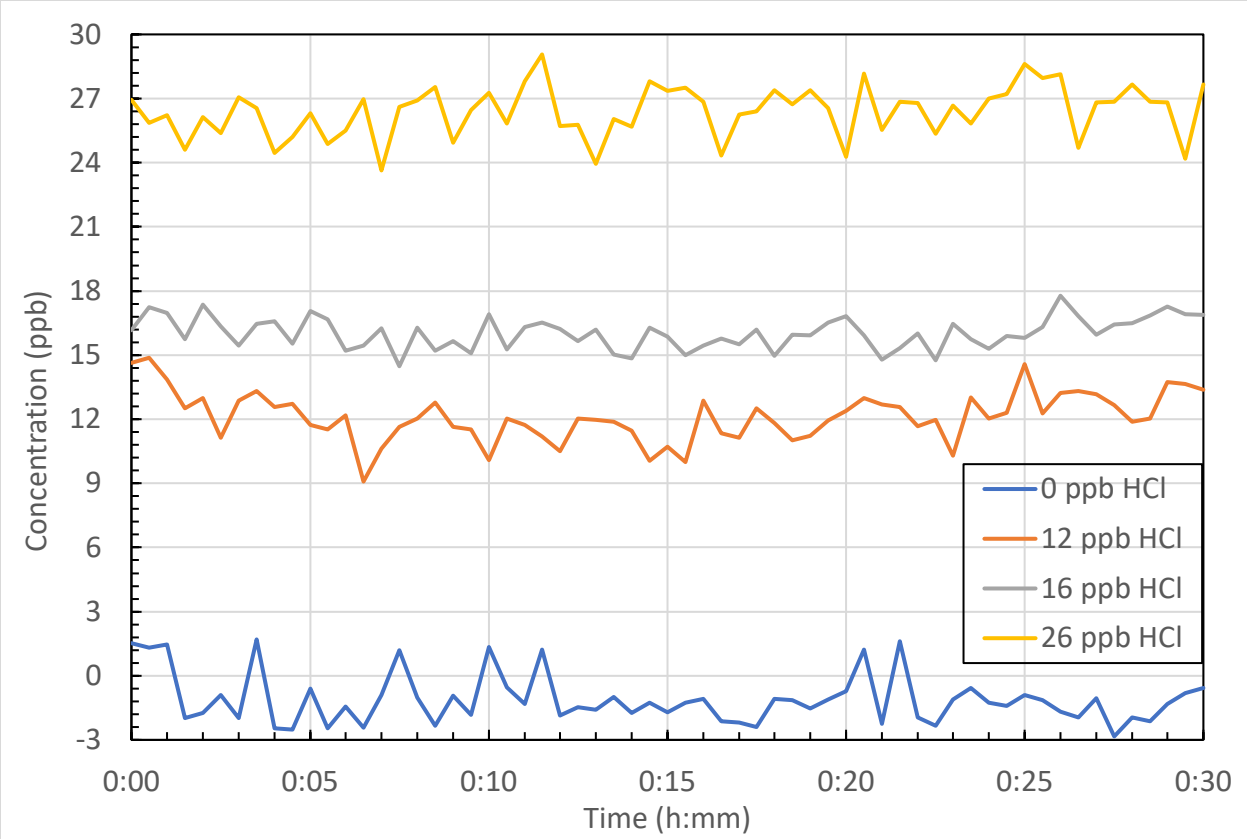

Figure 22: Examples of time-series of HCl concentration measurements by CRDS for (fitted) concentrations of ~0, 12, 16 and 26 ppb HCl.

4.1.2 Accuracy and Sensitivity

To determine the optimal integration (averaging) time for the CRDS system described, we conducted an Allan Variance analysis on a series of concentration measurements using a customized approach as outlined in Huang and Lehmann [80]. This modified method produced a significantly more refined Allan Variance curve when compared to the conventional two-sample variance approach. This provides a statistical method to analyze the measurement stability.

The capacity of a CRDS sensor to ascertain concentrations of trace atmospheric elements hinges on the optical precision of the instrument and the spectroscopic correlation between optical absorption and element concentration. While extended

integration times typically yield enhanced detection thresholds, eventually, system drift begins to dominate, leading to an optimal, finite integration time. Optical precision of the CRDS equipment used in our project is explored in the work of Hagen et al [45].

The Allan variance of the four tests shown above is shown in Figure 23. The Allan variance with an integration time of 30 seconds is about 1 ppb. For the 0 ppb case, the Allan variance exhibits a minimum of around 0.15 ppb at an optimal integration time of roughly 10 minutes while other concentrations show similar results (with <0.5 ppb at 10 minutes). These values demonstrate favorable performance compared to the typical HCl abundance in cleanroom environments targeted by the sensor. In most cases, the lowest Allan variance (of ~0.1-0.5 ppb) is found after ~600 s (10 minutes), representing the optimum integration time. This achieves our goal of detecting 1 ppb HCl or better for cleanroom purposes.

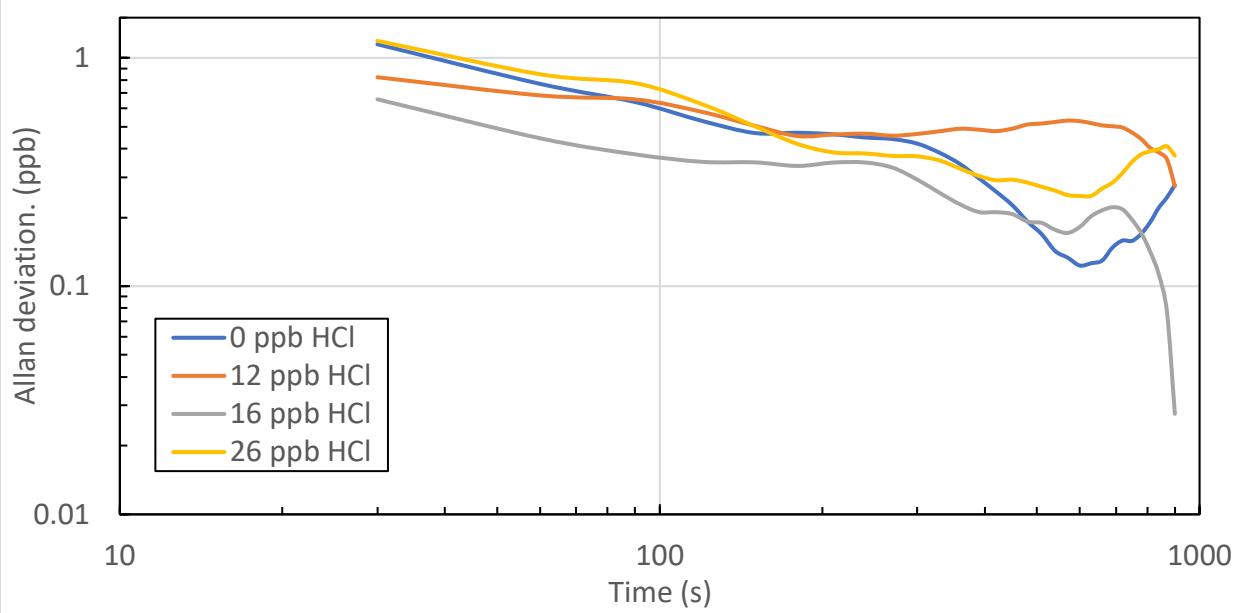

Figure 23: Allan variance of 0, 12, 16 and 26 ppb HCl respectively from top to bottom.

The detection limits achieved by the current open-path instrument underperform compared to the closed-path system tested by Hagen et al [45]. Even though we are

using all the same electronics and probing the same 2-0 band, the key difference is that they tested their equipment at less than 10^{th} of the atmospheric pressure and utilized a 90 cm cavity instead of a 60 cm cavity in our case.

4.2 Aerosol detection

The chamber was connected to a CPC (TSI Electrostatic Classifier 3082) to validate the ISO level within the chamber. We recorded multiple time-series of ring-down times and particle densities (ISO level) simultaneously. 15,000 ring-downs under constant ISO levels are extracted from these tests (15-20 minutes of data collection). These ring-downs are then fitted to cumulative distribution functions (cdf) and analyzed with standardized moments as described in section 3.5.3.

4.2.1 Mean Value (Center) Shifting

ISO levels would give higher ring-down (τ_0) times on average because of lower particle interaction loss. This showed some trends, but with a correlation coefficient of about 0.3, it was deemed too weak to be observed and deemed not useful (Figure 24).

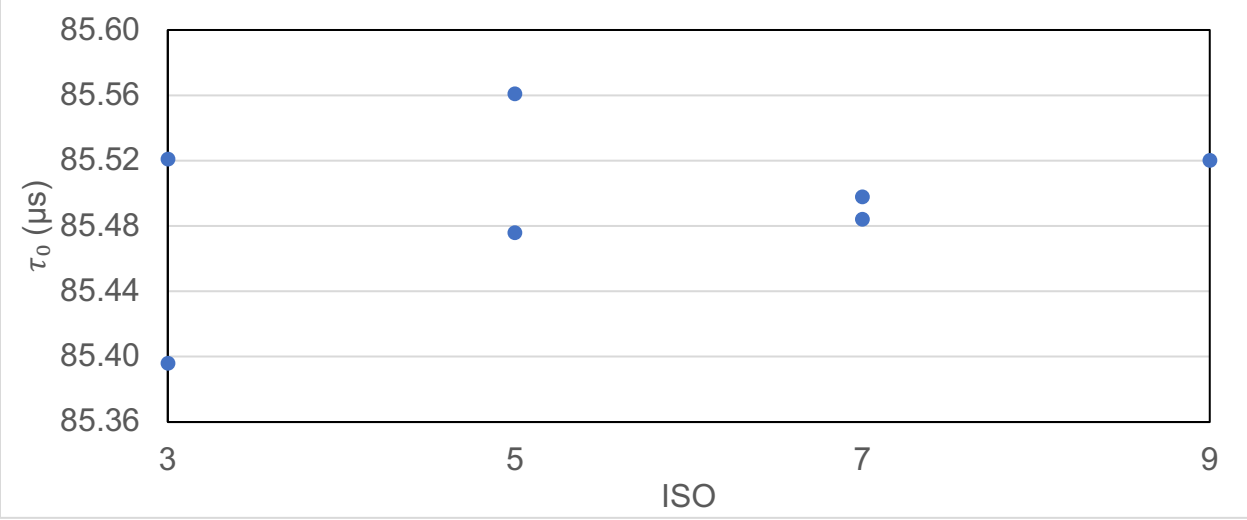

Figure 24: Very weak (unusable) correlation between increasing ring-down time with ISO level

Lower ISO should also give lower standard deviations but with a correlation coefficient of 0.25, this trend was very weak to observe (Figure 25).

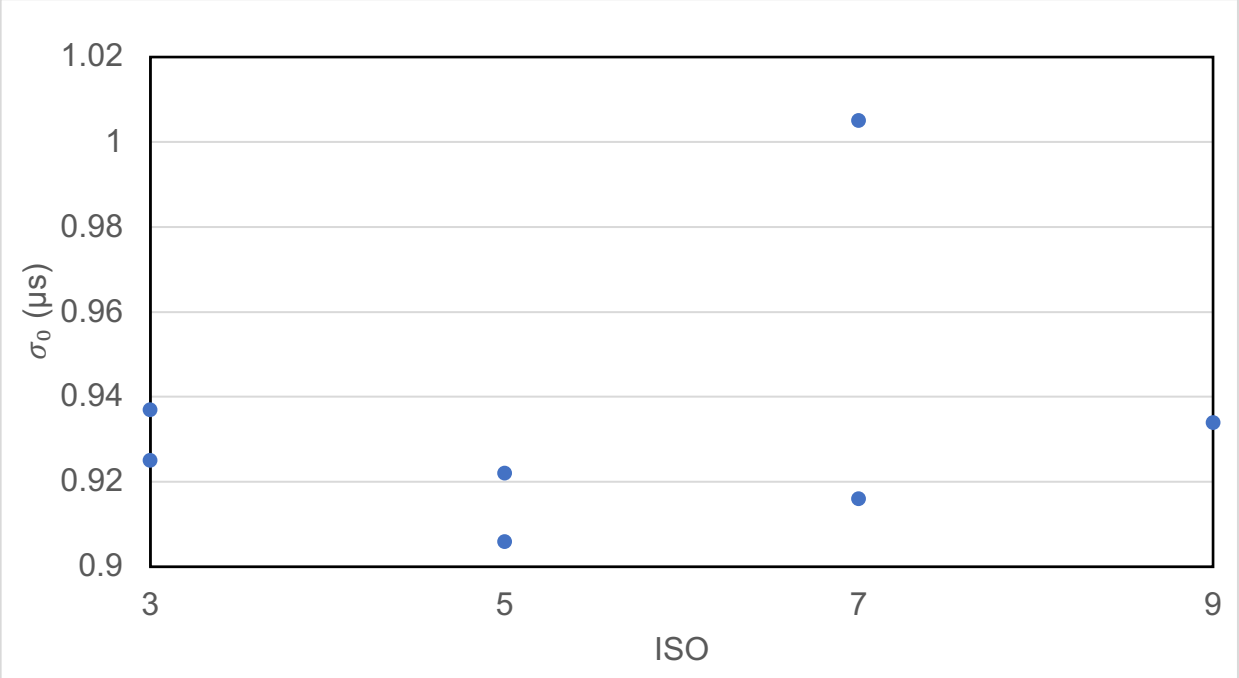

Figure 25: Very weak (unusable) correlation between standard deviation and ISO levels.

4.2.2 Outliers – cdf

Lower ISO gives fewer outliers, as quantified by the cumulative distribution function. Different values of δt were tested ranging from 2 µs to 4 µs This showed some trends with a correlation coefficient of about 0.77 but noise in ISO 3-5 makes it difficult to reliably detect ISO levels below ISO 5 (Figure 26).

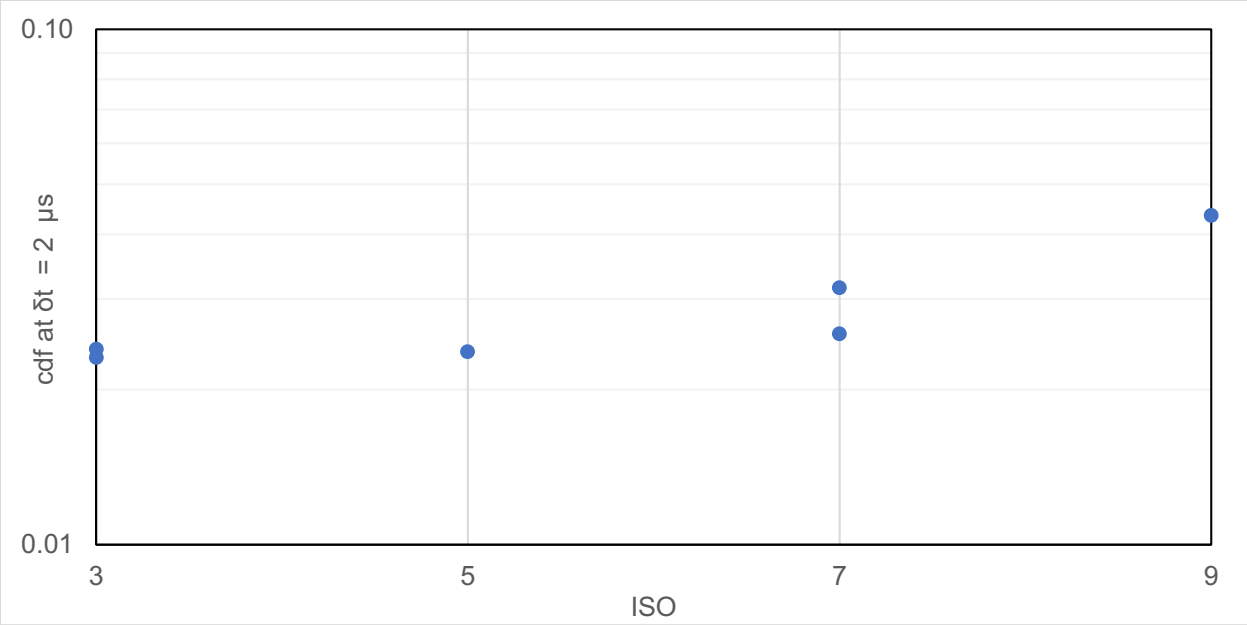

Figure 26: Good correlation between ISO level and multiple outlier points but ISO 3-5 is undistinguishable.

Similar tests in ISO 5-8 range produce better results with a stronger correlation coefficient of 0.85 (Figure 27).

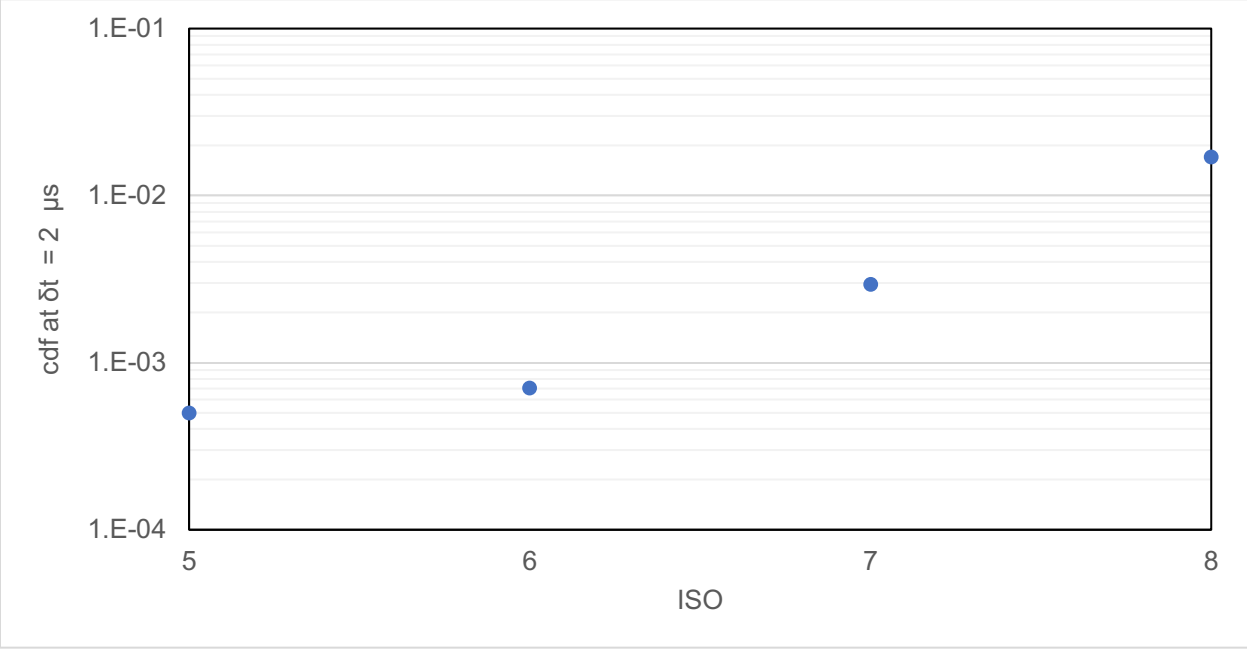

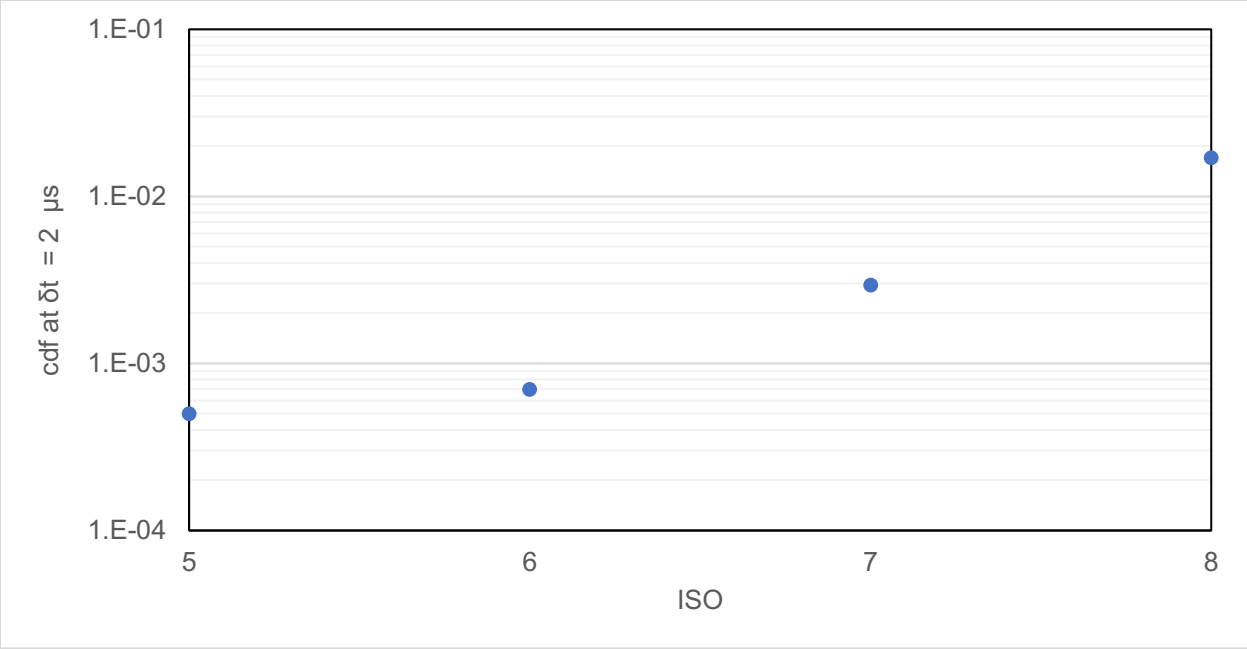

Figure 27: cdf outliers in ISO 5-8 range.

4.2.3 Distribution Shapes – Higher-Order Moments

Standardized moments provided us with further statistical analysis. Our results conclude that detection below ISO 5 is unreliable with absolute correlation coefficients of less than 0.84 (Figure 28). We have a stronger correlation for tests in ISO>5 and this can be utilized to characterize ISO levels or particle counts.

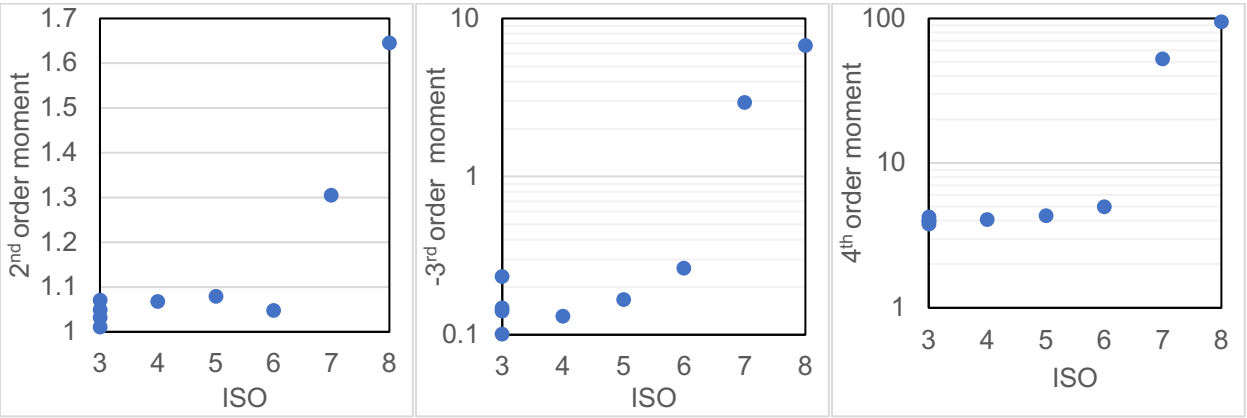

Figure 28: Higher-order standardized moments analysis on ISO 3-8

Focusing on ISO 5-ISO 8, we can conclude that the results from the ISO 5-8 characterization seem the most feasible with our equipment (Figure 29), with an

absolute correlation coefficient of > 0.9. This is especially robust with 3rd and 4th order moment analysis.

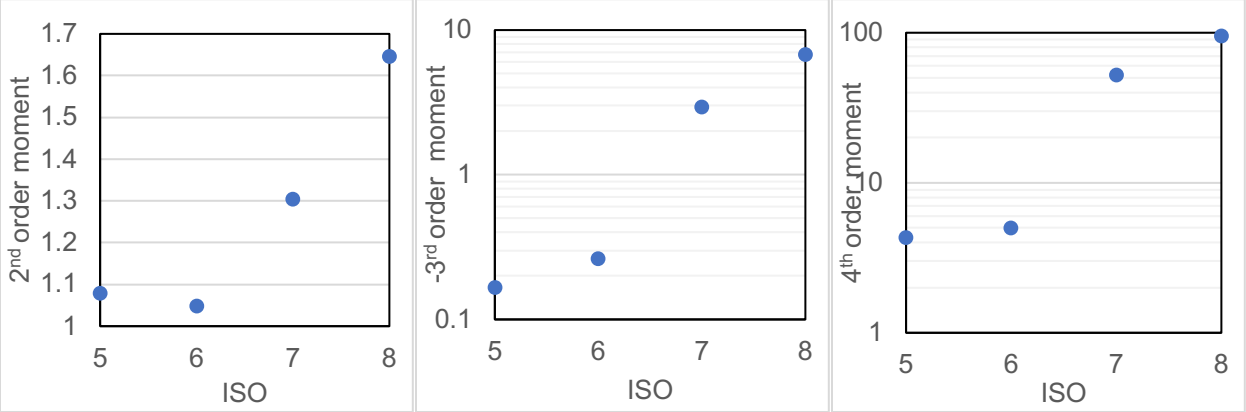

Figure 29: Higher-order moments for ISO 5-8 range show good correlation.

From our calculations, we find that on average every ring-down would interact with 0.05 particles in case of ISO 5 i.e. twenty ring-downs before any particle interaction. For higher-order ISO levels, we have a higher probability of multiple particle interactions within the same ring-down. Test results indicate that CRDS can quantify particle counts when there's multiple particle interactions with the laser beam. For smaller particle sizes, the optical loss due to particle interaction is so negligible that it is not discernable from noise. For a particle size of 0.3 μm, we only expect a ring-down time to increase by 0.03 μs, making it undetectable. However, their cumulative interaction within the same ring-down is detectable. ISO 5-8 characterization capability of our CRDS make them deployable in many cleanroom applications especially in sub-fab regions monitoring.

Chapter 5: Conclusions

The significance of this research is underscored by the global impact of silicon chips and their manufacturing requirement for cleanrooms. The cleanrooms have particular requirements for AMCs and aerosol concentration limits for the manufacturing of these chips. These limits can only reliably be achieved with robust monitoring. This study examines the ability of an open-path cavity ring-down-based sensor, primarily designed for application in cleanroom monitoring, to simultaneously detect trace levels of HCl (a representative AMC) and aerosols. The theoretical framework underpinning the detection method is delineated in Chapter 1, alongside a description of the distinctive features harnessed by the sensor in this thesis. Chapter 2 provides a precursor description of the distinctive features harnessed by the sensor in this thesis. Experimental methods and modifications made to enhance the sensor's functionality are presented in Chapter 3. Chapter 4 provides the results obtained and outlines sensor performance. The concluding sections summarize the findings from this thesis and lay out prospects for refining this sensor system.

5.1 Summary

A cost-effective set of NIR components, akin to those employed in the realm of telecommunications, were harnessed for crafting the apparatus. The performance metrics of our instrument should satisfy the requirements of numerous measurement campaigns and compare favorably to other devices. With a 30-second measurement time, our sensor can achieve a limit of detection (1σ) for HCl of around 1 ppb, which should be adequate for measurements in cleanroom conditions. This instrument exhibits

HCl detection thresholds in the realm of single digit ppbv, with the most effective integration durations hovering around approximately 10 minutes.

HCl has two primary isotopologues, $H^{35}Cl$ (75.76%) and $H^{37}Cl$ (24.23%). Our instrument directly measures the mixing ratio of $H^{35}Cl$, from which the overall HCl concentration is deduced. The R(4) line of $H^{37}Cl$ can also be measured without spectral interference, allowing for sensitive ambient measurements of the two dominant HCl isotopologues.

In addition to this, we've elucidated the operation of an aerosol quantification sensor that leverages the same cavity-enhanced absorption spectroscopy. Multiple hypotheses were tested as discussed earlier to characterize different ISO levels. With our setup, we can characterize cleanroom conditions in ≥ ISO 5 range. This is good for detecting particles in numerous cleanroom applications, especially the subfab region.

This versatility and validation tests make our instrument a promising tool for a wide range of applications. Its performance, combined with its capability to measure key isotopologues, positions it well for various research needs. In particular, it can be of significant value in many cleanroom monitoring applications, atmospheric studies, emissions monitoring, and environmental research. Indeed, our research sponsor (Samsung Electronics Corporation) has filed a provisional patent based on the approaches that have been developed here. Furthermore, our approach eliminates the need for specialized, cryogenically cooled components, simplifying instrument operation and maintenance. This reduction in complexity contributes to the ease of deployment in various settings, including cleanroom applications where adaptability and reconfiguration may be essential.

In summary, our work has introduced an HCl sensor with impressive detection capabilities and robust performance metrics, offering a valuable solution for accurately measuring HCl concentrations. Its versatility, precision, and suitability for various applications make it a significant advancement in the field of environmental and atmospheric monitoring. This instrument meets current research and SEC requirements and holds the potential for further advancements and innovative applications.

5.2 Future Work

From an optical perspective, there are several potential enhancements to consider regarding the photodetector within the cavity system. Initially, employing a detector and amplifier combination with a somewhat reduced bandwidth, around 400 kHz, could facilitate accurate measurement of the ring-down signal while simultaneously mitigating the adverse impacts of high-frequency noise. Additionally, the introduction of a thermoelectrically cooled photodiode may prove effective in minimizing dark noise originating from the detector. Currently its difficult to find a piece meeting all of our requirements but an example of this would be Thorlabs InGaAs amplified photodetector (PDA10D2). Furthermore, it’s plausible to achieve enhanced sensitivity through the utilization of more intricate CRDS configurations. However, this path comes at the cost of increased hardware complexity and expenses, for example, the integration of an external optical isolator (to reduce feedback from the cavity to the laser) or a more powerful laser. Another possible approach involves adopting a Pound-Drever-Hall locked cavity method akin to the approach described in the work of Paldus et al. [53]. In this approach, the frequencies of the laser and cavity are harmoniously synchronized, enabling the acquisition of ring-down data at higher rates, potentially reaching several

kilohertz. It's reasonable to anticipate a potential fivefold or greater improvement in detection sensitivity by incorporating this technique into the existing instrument; however, at the cost of increased system complexity, size and expense.

The existing system can identify neighboring spectral absorption lines associated with water and methane. Although these lines may not represent the most optimal choices for these particular molecules, detecting them in tandem with HCl remains feasible. Furthermore, straightforward modifications involving the laser, AOM, and cavity mirrors would enable the measurement of other NIR-absorbing substances, including CO, CO_2, and H_2S.

The closed aerosol test apparatus was conceived and developed following the "proof-of-concept" phase. Consequently, it has not yet undergone comprehensive characterization. Subsequent work should prioritize a deeper exploration of the flow dynamics within the control chamber to gain a deeper understanding of aerosol concentration distribution. Specifically, assumptions about uniform concentration across the laser sensing region need to be revisited, as significant losses due to factors such as the acrylic exoskeleton or variations in pressure within the dilution/vacuum flow subsystems could introduce a non-uniform concentration gradient. In a similar vein, scrutiny of the behavior of the CPC (Condensation Particle Counter) is warranted, as it might be selectively sampling in proximity to the laser sensing region, potentially leading to misleading results. Lastly, it is imperative to conduct thorough leak testing to confirm the absence of unintentional aerosol leakage or ingress of ambient air. Subsequently, a comprehensive assessment of the impact of the aerosol apparatus on the pre-existing optical setup is essential.

Characterizing the existing closed aerosol apparatus not only enhances the precision of aerosol measurements but also assists in the design of a more efficient instrument. Given that an initial characterization of the current setup has been carried out, the following suggestions for future enhancements are presented. To begin, constructing an improved test apparatus using steel material would be advantageous to mitigate concentration distribution issues stemming from the static charge associated with acrylic. Steel provides additional structural integrity, although it's worth noting that the utilization of this material presents some drawbacks, primarily related to cost and fabrication complexity. Furthermore, reducing the overall chamber size to decrease residence time is a valuable consideration. It's important to recognize that a larger aerosol flow rate is instrumental in reducing residence time.

For particle testing, an atomizer (or nebulizer) along with a fan inside the chamber can be utilized to create a polydisperse aerosol distribution, which can subsequently be dehydrated and introduced into the closed test chamber. This would greatly limit the fluctuations in particle count caused by other activities and lab experiments within the lab area. Furthermore, a more powerful laser source at a lower wavelength and with slight modifications to the CRDS system can help improve particle characterization at lower ISO levels. As discussed in chapter 2 a smaller wavelength, would increase the size parameter of aerosols and hence we will see more optical loss for smaller particle sizes making them easier to detect. This could still be an integrated system for an AMC that had absorption lines at higher frequencies. A longer cavity would increase the path length and, consequently, the scan area.

Bibliography

[1] “Airborne Molecular Contamination (AMC) Solutions for the Microelectronics Industry”.

[2] T. Pan and W. Wang, “From Cleanroom to Desktop: Emerging Micro-Nanofabrication Technology for Biomedical Applications,” *Ann. Biomed. Eng.*, vol. 39, no. 2, pp. 600–620, Feb. 2011, doi: 10.1007/s10439-010-0218-9.

[3] P. Naughton, “History of Cleanrooms,” *ASHRAE*, Nov. 2019, [Online]. Available: www.ashrae.org

[4] F. Wali, D. M. Knotter, and F. G. Kuper, “Impact of nano particles on semiconductor manufacturing,” in *2008 IEEE International Multitopic Conference*, Karachi: IEEE, Dec. 2008, pp. 97–99. doi: 10.1109/INMIC.2008.4777715.

[5] J. Li and Y.-F. Zhou, “Occupational hazards control of hazardous substances in clean room of semiconductor manufacturing plant using CFD analysis,” *Toxicol. Ind. Health*, vol. 31, no. 2, pp. 123–139, Feb. 2015, doi: 10.1177/0748233712469996.

[6] *Cleanrooms and associated controlled environments — Part 1: Classification of air cleanliness by particle concentration*, Dec. 15, 2015.

[7] B.-J. Wu, H. Bai, I.-K. Lin, and S. S. Liu, “Al–Cu Pattern Wafer Study on Metal Corrosion Due to Chloride Ion Contaminants,” *IEEE Trans. Semicond. Manuf.*, vol. 23, no. 4, pp. 553–558, Nov. 2010, doi: 10.1109/TSM.2010.2061972.

[8] T. Kamoshima *et al.*, “Controlling Ambient Gas in Slot-to-Slot Space Inside FOUP to Suppress Cu-Loss After Dual Damascene Patterning,” *IEEE Trans. Semicond. Manuf.*, vol. 21, no. 4, pp. 573–577, Nov. 2008, doi: 10.1109/TSM.2008.2005343.

[9] S. V. Sreenivasan, “Nanoimprint lithography steppers for volume fabrication of leading-edge semiconductor integrated circuits,” *Microsyst. Nanoeng.*, vol. 3, no. 1, p. 17075, Sep. 2017, doi: 10.1038/micronano.2017.75.

[10] G. Weineck, D. Zastera, and A. J. Dallas, “AMC control in photolithography: the past decade in review,” presented at the SPIE Advanced Lithography, C. J. Raymond, Ed., San Jose, California, Mar. 2010, p. 76383H. doi: 10.1117/12.847258.

[11] T. Conte, “INTERNATIONAL ROADMAP FOR DEVICES AND SYSTEMS.” IEEE, 2018.

[12] N. Pic *et al.*, “Defectivity decrease in the photolithography process by AMC level reduction through implementation of novel filtration and monitoring solutions,” presented at the SPIE Advanced Lithography, C. J. Raymond, Ed., San Jose, California, Mar. 2010, p. 76380M. doi: 10.1117/12.845591.

[13] A. Laskin, J. Laskin, and S. A. Nizkorodov, “Chemistry of Atmospheric Brown Carbon,” *Chem. Rev.*, vol. 115, no. 10, pp. 4335–4382, May 2015, doi: 10.1021/cr5006167.

[14] W. C. Hinds, *Aerosol technology: properties, behavior, and measurement of airborne particles*, 2nd ed. New York: Wiley, 1999.

[15] C. Clement, “Gas-to-particle conversion in the atmosphere: I. Evidence from empirical atmospheric aerosols,” *Atmos. Environ.*, vol. 33, no. 3, pp. 475–487, Feb. 1999, doi: 10.1016/S1352-2310(98)00264-7.

[16] I.-K. Lin, H. Bai, and B.-J. Wu, “Analysis of Relationship between Inorganic Gases and Fine Particles in Cleanroom Environment,” *Aerosol Air Qual. Res.*, vol. 10, no. 3, pp. 245–254, 2010, doi: 10.4209/aaqr.2009.10.0065.
[17] P. Garnier, Y. Borde, and G. Sevilla, “Airborne Molecular Contamination: Mechanism and Consequences on Devices,” *ECS Trans.*, vol. 108, no. 4, pp. 61–67, May 2022, doi: 10.1149/10804.0061ecst.
[18] B. Pelissier, A. Beaurain, H. Fontaine, A. Danel, and O. Joubert, “Investigations on HCl contaminated Cu 200 mm wafers using Parallel Angle Resolved XPS,” *Microelectron. Eng.*, vol. 86, no. 4–6, pp. 1013–1016, Apr. 2009, doi: 10.1016/j.mee.2009.01.025.
[19] C. Muller, “Comparison of Chemical Filters for the Control of Airborne Molecular Contamination,” *J. IEST*, vol. 50, no. 2, pp. 52–72, Oct. 2007, doi: 10.17764/jiet.50.2.n0256152322m4410.
[20] W. Den, H. Bai, and Y. Kang, “Organic Airborne Molecular Contamination in Semiconductor Fabrication Clean Rooms,” *J. Electrochem. Soc.*, vol. 153, no. 2, p. G149, 2006, doi: 10.1149/1.2147286.
[21] “The Rare Air of the Semiconductor Fab,” *Entegris*. Accessed: Jun. 26, 2023. [Online]. Available: https://www.entegris.com/en/home/resources/industry-insights/rare-air-semiconductor-fab.html
[22] S. A. MacDonald *et al.*, “Airborne chemical contamination of a chemically amplified resist,” presented at the Advances in Resist Technology and Processing VIII, H. Ito, Ed., San Jose, United States, Jun. 1991, pp. 2–12. doi: 10.1117/12.46354.
[23] K. Takeda, “Clean Technology Supporting Semiconductor Manufacturing Process. Evaluation and Analysis for Chemical Contamination.,” *J. Surf. Finish. Soc. Jpn.*, vol. 50, no. 10, pp. 887–893, 1999, doi: 10.4139/sfj.50.887.
[24] T.-S. Chuang and L.-M. Chang, “To mitigate airborne molecular contamination through ultra-pure air system,” *Build. Environ.*, vol. 59, pp. 153–163, Jan. 2013, doi: 10.1016/j.buildenv.2012.08.016.
[25] A. L. Moreno-Ríos, L. P. Tejeda-Benítez, and C. F. Bustillo-Lecompte, “Sources, characteristics, toxicity, and control of ultrafine particles: An overview,” *Geosci. Front.*, vol. 13, no. 1, p. 101147, Jan. 2022, doi: 10.1016/j.gsf.2021.101147.
[26] A. Peters, D. W. Dockery, J. E. Muller, and M. A. Mittleman, “Increased Particulate Air Pollution and the Triggering of Myocardial Infarction,” *Circulation*, vol. 103, no. 23, pp. 2810–2815, Jun. 2001, doi: 10.1161/01.CIR.103.23.2810.
[27] R. D. Brook *et al.*, “Particulate Matter Air Pollution and Cardiovascular Disease: An Update to the Scientific Statement From the American Heart Association,” *Circulation*, vol. 121, no. 21, pp. 2331–2378, Jun. 2010, doi: 10.1161/CIR.0b013e3181dbece1.
[28] “S. Korea’s SFA out to challenge Daifuku Technology,” *THE LEC*, Aug. 16, 2019. [Online]. Available: https://thelec.net/news/articleViewAmp.html?idxno=457
[29] R. W. Welker, “Size Analysis and Identification of Particles,” in *Developments in Surface Contamination and Cleaning*, Elsevier, 2012, pp. 179–213. doi: 10.1016/B978-1-4377-7883-0.00004-3.
[30] M. Heim, B. J. Mullins, H. Umhauer, and G. Kasper, “Performance evaluation of three optical particle counters with an efficient ‘multimodal’ calibration method,” *J.*

Aerosol Sci., vol. 39, no. 12, pp. 1019–1031, Dec. 2008, doi: 10.1016/j.jaerosci.2008.07.006.
[31] D. Wimmer *et al.*, “Performance of diethylene glycol-based particle counters in the sub-3 nm size range,” *Atmospheric Meas. Tech.*, vol. 6, no. 7, pp. 1793–1804, Jul. 2013, doi: 10.5194/amt-6-1793-2013.
[32] S. V. Hering, M. R. Stolzenburg, F. R. Quant, D. R. Oberreit, and P. B. Keady, “A Laminar-Flow, Water-Based Condensation Particle Counter (WCPC),” *Aerosol Sci. Technol.*, vol. 39, no. 7, pp. 659–672, Jul. 2005, doi: 10.1080/02786820500182123.
[33] J. Volckens and T. M. Peters, “Counting and particle transmission efficiency of the aerodynamic particle sizer,” *J. Aerosol Sci.*, vol. 36, no. 12, pp. 1400–1408, Dec. 2005, doi: 10.1016/j.jaerosci.2005.03.009.
[34] “AERODYNAMIC PARTICLE SIZER® MODEL 3321 THEORY OF OPERATION.” TSI Incorporated.
[35] Y. Wang, J. Li, H. Jing, Q. Zhang, J. Jiang, and P. Biswas, “Laboratory Evaluation and Calibration of Three Low-Cost Particle Sensors for Particulate Matter Measurement,” *Aerosol Sci. Technol.*, vol. 49, no. 11, pp. 1063–1077, Nov. 2015, doi: 10.1080/02786826.2015.1100710.
[36] Q. G. J. Malloy *et al.*, “Real-Time Aerosol Density Determination Utilizing a Modified Scanning Mobility Particle Sizer—Aerosol Particle Mass Analyzer System,” *Aerosol Sci. Technol.*, vol. 43, no. 7, pp. 673–678, Jun. 2009, doi: 10.1080/02786820902832960.
[37] D. Harvey, *Modern analytical chemistry*. Boston: McGraw-Hill, 2000.
[38] S. Eliuk and A. Makarov, “Evolution of Orbitrap Mass Spectrometry Instrumentation,” *Annu. Rev. Anal. Chem.*, vol. 8, no. 1, pp. 61–80, Jul. 2015, doi: 10.1146/annurev-anchem-071114-040325.
[39] P. R. Griffiths and J. A. De Haseth, *Fourier transform infrared spectrometry*, 2nd ed. in Chemical analysis, no. v. 171. Hoboken, N.J: Wiley-Interscience, 2007.
[40] J. E. Lovelock, “A Photoionization Detector for Gases and Vapours,” *Nature*, vol. 188, no. 4748, pp. 401–401, Oct. 1960, doi: 10.1038/188401a0.
[41] T. P. Forbes and R. Burks, “Field-Deployable Devices,” in *Encyclopedia of Forensic Sciences, Third Edition*, Elsevier, 2023, pp. 413–423. doi: 10.1016/B978-0-12-823677-2.00060-X.
[42] C. O. Park, J. W. Fergus, N. Miura, J. Park, and A. Choi, “Solid-state electrochemical gas sensors,” *Ionics*, vol. 15, no. 3, pp. 261–284, Jun. 2009, doi: 10.1007/s11581-008-0300-6.
[43] T.-V. Dinh, I.-Y. Choi, Y.-S. Son, and J.-C. Kim, “A review on non-dispersive infrared gas sensors: Improvement of sensor detection limit and interference correction,” *Sens. Actuators B Chem.*, vol. 231, pp. 529–538, Aug. 2016, doi: 10.1016/j.snb.2016.03.040.
[44] J. G. Irwin and M. L. Williams, “Acid rain: Chemistry and transport,” *Environ. Pollut.*, vol. 50, no. 1–2, pp. 29–59, 1988, doi: 10.1016/0269-7491(88)90184-4.
[45] C. L. Hagen *et al.*, “Cavity ring-down spectroscopy sensor for detection of hydrogen chloride,” *Atmospheric Meas. Tech.*, vol. 7, no. 2, pp. 345–357, Feb. 2014, doi: 10.5194/amt-7-345-2014.

[46] E. Scheuer, “Seasonal distributions of fine aerosol sulfate in the North American Arctic basin during TOPSE,” *J. Geophys. Res.*, vol. 108, no. D4, p. 8370, 2003, doi: 10.1029/2001JD001364.
[47] W. C. Keene, J. R. Maben, A. A. P. Pszenny, and J. N. Galloway, “Measurement technique for inorganic chlorine gases in the marine boundary layer,” *Environ. Sci. Technol.*, vol. 27, no. 5, pp. 866–874, May 1993, doi: 10.1021/es00042a008.
[48] P. Veres *et al.*, “Development of negative-ion proton-transfer chemical-ionization mass spectrometry (NI-PT-CIMS) for the measurement of gas-phase organic acids in the atmosphere,” *Int. J. Mass Spectrom.*, vol. 274, no. 1–3, pp. 48–55, Jul. 2008, doi: 10.1016/j.ijms.2008.04.032.
[49] S. Kim *et al.*, “Airborne measurements of HCl from the marine boundary layer to the lower stratosphere over the North Pacific Ocean during INTEX-B,” preprint, Feb. 2008. doi: 10.5194/acpd-8-3563-2008.
[50] T. P. Marcy *et al.*, “Quantifying Stratospheric Ozone in the Upper Troposphere with in Situ Measurements of HCl,” *Science*, vol. 304, no. 5668, pp. 261–265, Apr. 2004, doi: 10.1126/science.1093418.
[51] A. O’Keefe and D. A. G. Deacon, “Cavity ring-down optical spectrometer for absorption measurements using pulsed laser sources,” *Rev. Sci. Instrum.*, vol. 59, no. 12, pp. 2544–2551, Dec. 1988, doi: 10.1063/1.1139895.
[52] K. K. Lehmann, G. Berden, and R. Engeln, “An Introduction to Cavity Ring-Down Spectroscopy,” in *Cavity Ring-Down Spectroscopy*, G. Berden and R. Engeln, Eds., Chichester, UK: John Wiley & Sons, Ltd, 2009, pp. 1–26. doi: 10.1002/9781444308259.ch1.
[53] B. A. Paldus and A. A. Kachanov, “An historical overview of cavity-enhanced methods,” *Can. J. Phys.*, vol. 83, no. 10, pp. 975–999, Oct. 2005, doi: 10.1139/p05-054.
[54] D. Z. Anderson, J. C. Frisch, and C. S. Masser, “Mirror reflectometer based on optical cavity decay time,” *Appl. Opt.*, vol. 23, no. 8, p. 1238, Apr. 1984, doi: 10.1364/AO.23.001238.
[55] J. J. Scherer, J. B. Paul, A. O’Keefe, and R. J. Saykally, “Cavity Ringdown Laser Absorption Spectroscopy: History, Development, and Application to Pulsed Molecular Beams,” *Chem. Rev.*, vol. 97, no. 1, pp. 25–52, Feb. 1997, doi: 10.1021/cr930048d.
[56] A. Maity, S. Maithani, and M. Pradhan, “Cavity ring-down spectroscopy: recent technological advances and applications,” in *Molecular and Laser Spectroscopy*, Elsevier, 2020, pp. 83–120. doi: 10.1016/B978-0-12-818870-5.00003-4.
[57] D. Romanini, A. A. Kachanov, N. Sadeghi, and F. Stoeckel, “CW cavity ring down spectroscopy,” *Chem. Phys. Lett.*, vol. 264, no. 3–4, pp. 316–322, Jan. 1997, doi: 10.1016/S0009-2614(96)01351-6.
[58] D. Romanini, A. A. Kachanov, and F. Stoeckel, “Diode laser cavity ring down spectroscopy,” *Chem. Phys. Lett.*, vol. 270, no. 5–6, pp. 538–545, May 1997, doi: 10.1016/S0009-2614(97)00406-5.
[59] R. Paschotta, “Acousto-optic Modulators - an encyclopedia article,” in *RP Photonics Encyclopedia*, RP Photonics AG, 2008. doi: 10.61835/az1.
[60] J. B. Dudek, P. B. Tarsa, A. Velasquez, M. Wladyslawski, P. Rabinowitz, and K. K. Lehmann, “Trace Moisture Detection Using Continuous-Wave Cavity Ring-Down

Spectroscopy," *Anal. Chem.*, vol. 75, no. 17, pp. 4599–4605, Sep. 2003, doi: 10.1021/ac0343073.
[61] L. E. Mchale, B. Martinez, T. W. Miller, and A. P. Yalin, "Open-path cavity ring-down methane sensor for mobile monitoring of natural gas emissions," *Opt. Express*, vol. 27, no. 14, p. 20084, Jul. 2019, doi: 10.1364/OE.27.020084.
[62] H. Panu *et al.*, "Real-time HCl gas detection at parts-per-billion level concentrations utilising a diode laser and a bismuth-doped fibre amplifier," *Meas. Sci. Technol.*, vol. 32, no. 5, p. 055206, May 2021, doi: 10.1088/1361-6501/abd651.
[63] J. Wilkerson *et al.*, "In situ observations of stratospheric HCl using three-mirrorintegrated cavity output spectroscopy," Gases/In Situ Measurement/Instruments and Platforms, preprint, Feb. 2021. doi: 10.5194/amt-2021-6.
[64] G. Mie, "Beiträge zur Optik trüber Medien, speziell kolloidaler Metallösungen," *Ann. Phys.*, vol. 330, no. 3, pp. 377–445, Jan. 1908, doi: 10.1002/andp.19083300302.
[65] "Light scattering by small particles. By H. C. van de Hulst. New York (John Wiley and Sons), London (Chapman and Hall), 1957. Pp. xiii, 470; 103 Figs.; 46 Tables. 96s," *Q. J. R. Meteorol. Soc.*, vol. 84, no. 360, pp. 198–199, Apr. 1958, doi: 10.1002/qj.49708436025.
[66] M. Kerker, *The scattering of light and other electromagnetic radiation*. in Physical chemistry, no. 16. New York [etc.]: Academic Press, 1969.
[67] J. Li *et al.*, "Scattering and absorbing aerosols in the climate system," *Nat. Rev. Earth Environ.*, vol. 3, no. 6, pp. 363–379, May 2022, doi: 10.1038/s43017-022-00296-7.
[68] J. Brewer, S. Kulkarni, and A. P. Raman, "Resonant Anti-Reflection Metasurfaces for Infrared Transmission Optics," *Nano Lett.*, vol. 23, no. 19, pp. 8940–8946, Oct. 2023, doi: 10.1021/acs.nanolett.3c02375.
[69] P. M. Carvalho, M. R. Felício, N. C. Santos, S. Gonçalves, and M. M. Domingues, "Application of Light Scattering Techniques to Nanoparticle Characterization and Development," *Front. Chem.*, vol. 6, p. 237, Jun. 2018, doi: 10.3389/fchem.2018.00237.
[70] L. E. McHale, A. Hecobian, and A. P. Yalin, "Open-path cavity ring-down spectroscopy for trace gas measurements in ambient air," *Opt. Express*, vol. 24, no. 5, p. 5523, Mar. 2016, doi: 10.1364/OE.24.005523.
[71] A. A. Riziq, C. Erlick, E. Dinar, and Y. Rudich, "Optical properties of absorbing and non-absorbing aerosols retrieved by cavity ring down (CRD) spectroscopy," *Atmos Chem Phys*, 2007.
[72] B. J. Mason, J. S. Walker, J. P. Reid, and A. J. Orr-Ewing, "Deviations from Plane-Wave Mie Scattering and Precise Retrieval of Refractive Index for a Single Spherical Particle in an Optical Cavity," *J. Phys. Chem. A*, vol. 118, no. 11, pp. 2083–2088, Mar. 2014, doi: 10.1021/jp5014863.
[73] T. D. Gordon *et al.*, "Design of a Novel Open-Path Aerosol Extinction Cavity Ringdown Spectrometer," *Aerosol Sci. Technol.*, vol. 49, no. 9, pp. 717–726, Sep. 2015, doi: 10.1080/02786826.2015.1066753.
[74] J. M. Langridge, M. S. Richardson, D. Lack, D. Law, and D. M. Murphy, "Aircraft Instrument for Comprehensive Characterization of Aerosol Optical Properties, Part I: Wavelength-Dependent Optical Extinction and Its Relative Humidity Dependence

Measured Using Cavity Ringdown Spectroscopy," *Aerosol Sci. Technol.*, vol. 45, no. 11, pp. 1305–1318, Nov. 2011, doi: 10.1080/02786826.2011.592745.
[75] P. Weibring, D. Richter, J. G. Walega, L. Rippe, and A. Fried, "Difference frequency generation spectrometer for simultaneous multispecies detection," *Opt. Express*, vol. 18, no. 26, p. 27670, Dec. 2010, doi: 10.1364/OE.18.027670.
[76] L. S. Rothman *et al.*, "The HITRAN2012 molecular spectroscopic database," *J. Quant. Spectrosc. Radiat. Transf.*, vol. 130, pp. 4–50, Nov. 2013, doi: 10.1016/j.jqsrt.2013.07.002.
[77] P. Ortwein, W. Woiwode, S. Wagner, M. Gisi, and V. Ebert, "Laser-based measurements of line strength, self- and pressure-broadening coefficients of the H35Cl R(3) absorption line in the first overtone region for pressures up to 1 MPa," *Appl. Phys. B*, vol. 100, no. 2, pp. 341–347, Aug. 2010, doi: 10.1007/s00340-009-3862-8.
[78] W. Feller, *An introduction to probability theory and its applications. Vol. 1*, 3. ed., rev. Print., [Nachdr.]., vol. 1. in Wiley series in probability and mathematical statistics, vol. 1. S.l.: Wiley, 2009.
[79] A. Papoulis, *Probability, random variables, and stochastic processes*, 2nd ed. in McGraw-Hill series in electrical engineering. New York: McGraw-Hill, 1984.
[80] H. Huang and K. K. Lehmann, "Sensitivity Limits of Continuous Wave Cavity Ring-Down Spectroscopy," *J. Phys. Chem. A*, vol. 117, no. 50, pp. 13399–13411, Dec. 2013, doi: 10.1021/jp406691e.